Cell Reports
Medicine

Article

Proteomics separates adult-type diffuse high-grade gliomas in metabolic subgroups independent of 1p/19q codeletion and across IDH mutational status

Graphical abstract

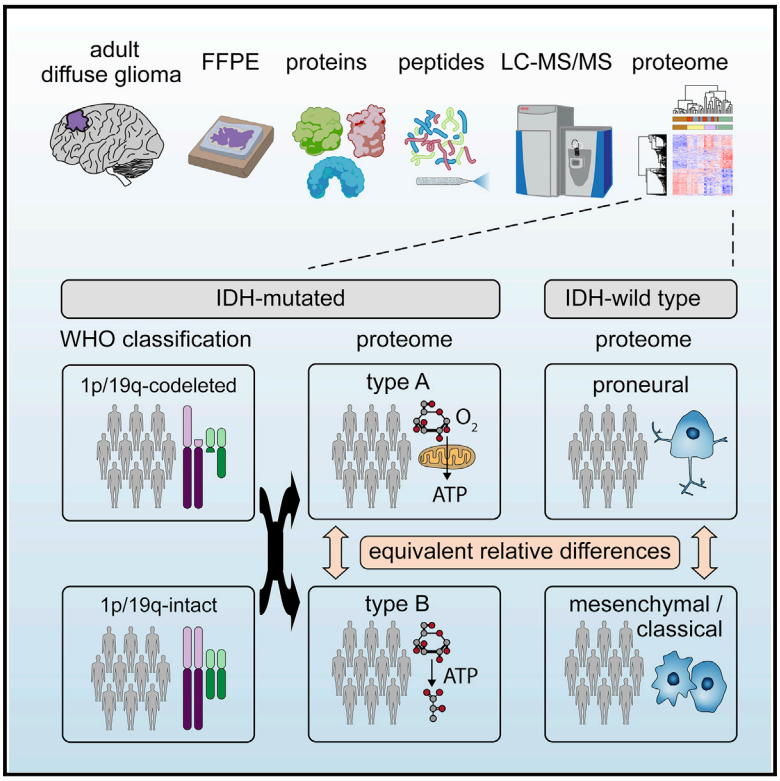

Highlights

- The tumor proteomes of IDHmut gliomas do not segregate by 1p/19q codeletion
- IDHmut gliomas show two aerobic/anaerobic energy metabolism subgroups
- Metabolic IDHmut subgroups resemble proneural and mesenchymal/classic IDHwt glioma
- Protein level perturbations of oncogenes and tumor suppressors in glioma

Authors

Jakob Maximilian Bader, Nikolaus Deigendesch, Martin Misch, Matthias Mann, Arend Koch, Felix Meissner

Correspondence

arend.koch@charite.de (A.K.), felix.meissner@uni-bonn.de (F.M.)

In brief

Bader et al. use liquid chromatography-mass spectrometry to characterize the proteomes of diffuse glioma brain tumors. The study reveals that Isocitrate dehydrogenase-mutant gliomas segregate into two metabolic subtypes resembling proneural and classic/mesenchymal subtypes in Isocitrate dehydrogenase wild-type gliomas. This has broad implications for clinical patient stratification and therapy.

Bader et al., 2023, Cell Reports Medicine *4*, 100877
January 17, 2023
https://doi.org/10.1016/j.xcrm.2022.100877

CellPress

Cell Reports Medicine

CellPress
OPEN ACCESS

Article

Proteomics separates adult-type diffuse high-grade gliomas in metabolic subgroups independent of 1p/19q codeletion and across IDH mutational status

Jakob Maximilian Bader,[1] Nikolaus Deigendesch,[2] Martin Misch,[3] Matthias Mann,[1,4] Arend Koch,[5,7,*] and Felix Meissner[1,6,7,8,*]

[1]Department of Proteomics and Signal Transduction, Max Planck Institute of Biochemistry, 82152 Martinsried, Germany
[2]Pathology, Institute of Medical Genetics and Pathology, University Hospital Basel, University of Basel, 4031 Basel, Switzerland
[3]Department of Neurosurgery, Charité, Universitätsmedizin Berlin Corporate Member of Freie Universität Berlin, and Humboldt-Universität zu Berlin, Berlin Institute of Health, 13353 Berlin, Germany
[4]Novo Nordisk Foundation Center for Protein Research, Faculty of Health Sciences, University of Copenhagen, 2200 Copenhagen, Denmark
[5]Department of Neuropathology, Charité, Universitätsmedizin Berlin Corporate Member of Freie Universität Berlin, and Humboldt-Universität zu Berlin, Berlin Institute of Health, 13353 Berlin, Germany
[6]Department of Systems Immunology and Proteomics, Institute of Innate Immunity, University Hospital Bonn, 53127 Bonn, Germany
[7]These authors contributed equally
[8]Lead contact
*Correspondence: arend.koch@charite.de (A.K.), felix.meissner@uni-bonn.de (F.M.)
https://doi.org/10.1016/j.xcrm.2022.100877

SUMMARY

High-grade adult-type diffuse gliomas are malignant neuroepithelial tumors with poor survival rates in combined chemoradiotherapy. The current WHO classification is based on IDH1/2 mutational and 1p/19q codeletion status. Glioma proteome alterations remain undercharacterized despite their promise for a better molecular patient stratification and therapeutic target identification. Here, we use mass spectrometry to characterize 42 formalin-fixed, paraffin-embedded (FFPE) samples from IDH-wild-type (IDHwt) gliomas, IDH-mutant (IDHmut) gliomas with and without 1p/19q codeletion, and non-neoplastic controls. Based on more than 5,500 quantified proteins and 5,000 phosphosites, gliomas separate by IDH1/2 mutational status but not by 1p/19q status. Instead, IDHmut gliomas split into two proteomic subtypes with widespread perturbations, including aerobic/anaerobic energy metabolism. Validations with three independent glioma proteome datasets confirm these subgroups and link the IDHmut subtypes to the established proneural and classic/mesenchymal subtypes in IDHwt glioma. This demonstrates common phenotypic subtypes across the IDH status with potential therapeutic implications for patients with IDHmut gliomas.

INTRODUCTION

Gliomas in adulthood account for about 80% of malignant primary brain tumors with an incidence of about 5 per 100,000 people.[1] In general, adult diffuse gliomas are classified according to histomorphological and molecular characteristics, including isocitrate dehydrogenase (IDH) mutations and 1p/19q codeletions, and graded (WHO grades 2 to 4) for predicting clinical-biological behavior (WHO Classification of Central Nervous System Tumours, fifth edition[2]). The category of adult diffuse gliomas comprises astrocytoma, IDH-mutant (IDHmut), oligodendroglioma, IDHmut and 1p/19q codeleted, and glioblastoma, IDH-wild-type (IDHwt). Most IDHwt glioblastoma patients die within 15–18 months after diagnosis and the 5-year survival rate does not exceed 10% despite therapy,[3,4] while astrocytoma, IDH-mutant, have a significantly better prognosis. Unfortunately, the overall survival has not been improved markedly in recent years.

Several genetic alterations in the development and progression of diffuse gliomas have been known for years.[5] Key genetic events include hotspot mutations in IDH genes 1 and 2 and codeletion of the 1p/19q chromosome arms. The molecular genetics are routinely assessed in clinical practice for diagnostic purposes as both are associated with prognostic and predictive relevance.[6,7] Mechanistically, missense mutations alter IDH enzymatic activity such that the oncometabolite D-2-hydroxyglutarate is formed, which leads to epigenetic remodeling via demethylase inhibition and HIF1-dependent survival and angiogenesis.[8] Codeletion of 1p/19q occurs in IDHmut oligodendrogliomas but not in astrocytomas; however, its pathological mechanism is less well understood.[9,10]

Omics technologies have emerged as powerful methods to classify gliomas. Genomic and transcriptomic analyses revealed subtypes of high-grade gliomas with decreasing survival, which are referred to as proneural, classical, and mesenchymal.[11,12]

Further integrative genomic, transcriptomic, and epigenomic analyses of gliomas WHO grades 2 to 4 indicated at least seven glioma subtypes, with the most prominent classifier being IDH mutational status.[13] IDHmut gliomas further separated into a 1p/19q codeletion entity and two non-codeletion entities, namely high and low glioma CpG island methylation phenotype. Notably, the classification of IDHwt gliomas was largely orthogonal to the previous GBM classification, suggesting greater complexity. In addition, methylation-based classification of CNS tumors revealed 82 distinct tumor methylation classes.[14]

Genome-wide epigenetics and next-generation sequencing of tumor genomes have lately found their way into routine neuropathological diagnostics. Nevertheless, the scientific community has continued to improve the classification of IDHmut gliomas focusing on non-1p/19q codeleted astrocytomas and recently identified CDKN2A/B status as a biomarker.[15] Despite these advances in the biological subclassification of CNS tumor entities, there have been no significant breakthroughs in tumor therapy for high-grade gliomas in recent years. Thus, it remains an unmet need to refine the classification of gliomas and to identify cellular targets for future therapies.

In contrast to the advances in the epigenetic, genetic, and transcriptomic characterization of gliomas, an equivalent understanding at the proteome level has not yet been achieved. Mass spectrometry (MS) has emerged as the method of choice for large-scale proteome investigations with many applications in biology and medicine.[16] However, previous studies utilizing MS to analyze the human glioma proteome often covered few proteins, were limited to available fresh tumor tissue, or were conducted with immortalized cell lines. We have demonstrated previously that several thousand proteins can be robustly quantified from formalin-fixed, paraffin-embedded (FFPE) tissue, making a plethora of biobank samples amenable to proteomic analysis.[17,18] Moreover, the analysis of the phosphoproteome can reveal altered signaling checkpoints of cancerous transformation across all areas of cell biology. Phosphotyrosine signaling has been shown to be preserved in FFPE samples, and the phosphoproteome of FFPE samples, including cancer tissues, has been investigated before.[19–21] Inspired by recent proteomic and phosphoproteomic studies proving its potential to stratify breast cancer subtypes,[22–24] we set out to characterize the proteomes of adult-type diffuse high-grade gliomas.

RESULTS

Sample characteristics and proteomic workflow

We collected 10 to 11 FFPE samples of glioblastoma, IDHwt; oligodendroglioma IDH-mutant and 1p/19q-codeleted (codel); astrocytoma IDH-mutant (non-codel); and 10 control samples of non-neoplastic CNS tissue (CNS ctrl) (Figure 1A; Table 1). All tumors were classified histomorphologically and immunohistochemically according to the criteria of the WHO classification for CNS tumors (fifth edition). In addition, we characterized all tumors (epi)genetically using genome-wide methylation profiling and copy number variation (CNV) profiling.

We applied an FFPE proteomics workflow that we established previously and used to analyze ovarian cancer subtypes.[17] FFPE slices were deparaffinized, homogenized, and protein extracts were digested by trypsin and LysC. Peptides were subjected to liquid chromatography-tandem mass spectrometry (LC-MS/MS) analysis or used for phosphopeptide enrichment and subsequent LC-MS/MS analysis (Figure 1A). Our dataset comprised a total of 5,724 proteins and 5,212 high-confidence phosphosites, corresponding to about 5,000 quantified proteins and 3,000 phosphosites per sample (Figure S1A).

Global dataset structure and IDHwt/IDHmut glioma proteome differences

We assessed the molecular relationship of tumor proteomes by unbiased hierarchical clustering and principal-component analysis and linked main proteome differences to biological pathways (Figures 1B–1D).

The CNS ctrls clustered most closely and clearly separated from the gliomas (Figures 1B and 1C). Compared with both IDHwt and IDHmut glioma, the CNS ctrls were enriched in synaptic and myelin-related proteins, reflective of functional brain tissue in good quantitative concordance with CPTAC glioma proteome data (Figures 1D and S1B).[25]

The IDHwt gliomas in our study were most distinct from CNS ctrl and also segregated from IDHmut gliomas (Figures 1B and 1C). The IDHwt proteome was enriched with proteins linked to inflammation, MCM complex DNA polymerases, an integrin-, collagen-, and laminin-rich "basement membrane-like" extracellular matrix (ECM) profile, low in hyaluronic acid, which is associated with increased malignancy in gliomas (Figures 1C–1E).[26] IDHwt/IDHmut differences aligned well with the CPTAC data and were largely unaffected by 1p/19q codeletion status in our data (Figures 1E, S1C, and S1D). In line with a more "aggressive" phenotype of IDHwt gliomas, many outlier proteins with high abundance in IDHwt are cancer drivers, several of them linked to invasion. Outlier proteins associated with IDHmut included tumor suppressors downregulated in IDHwt (Figures 1E and S1D; Table 2). Notably, these tumor suppressors include the histone proteins H1F0 and H2AFY2, which both maintain an epigenetic profile of differentiation and inhibit a return to a proliferative stem cell state through distinct mechanisms.[27,28] Known proteome alterations driving progression of the IDHmut were apparent, such as the strong epigenetic downregulation of RBP1, as well as novel ones, such as AKR1C3 overexpression selectively in IDHmut (Figures 1E and S1E; Table 2).

Intriguingly, the IDHmut gliomas did not separate according to the codeletion status in a hierarchical cluster and in the first two principal components, indicating a minor effect of the codeletion status on the proteome (Figures 1B–1C and S1F). Instead, the IDHmut gliomas reproducibly fall into two distinct clusters, which were balanced for the codeletion status and patient gender (Figures 1A–1C and S1G). We refer to them as HGG-IDHmut-A and HGG-IDHmut-B. HGG-IDHmut-A formed a cluster, which was more similar to CNS ctrls than to other gliomas (Figures 1B and 1C). HGG-IDHmut-B formed a more diffuse cluster which was most related to IDHwt glioma.

HGG-IDHmut-A/B sub-stratification is independent of epigenetic profile, CNV alterations, or clinical parameters

We carefully examined potential sources of systematic biases in our study groups. First, we compared the proteome-based

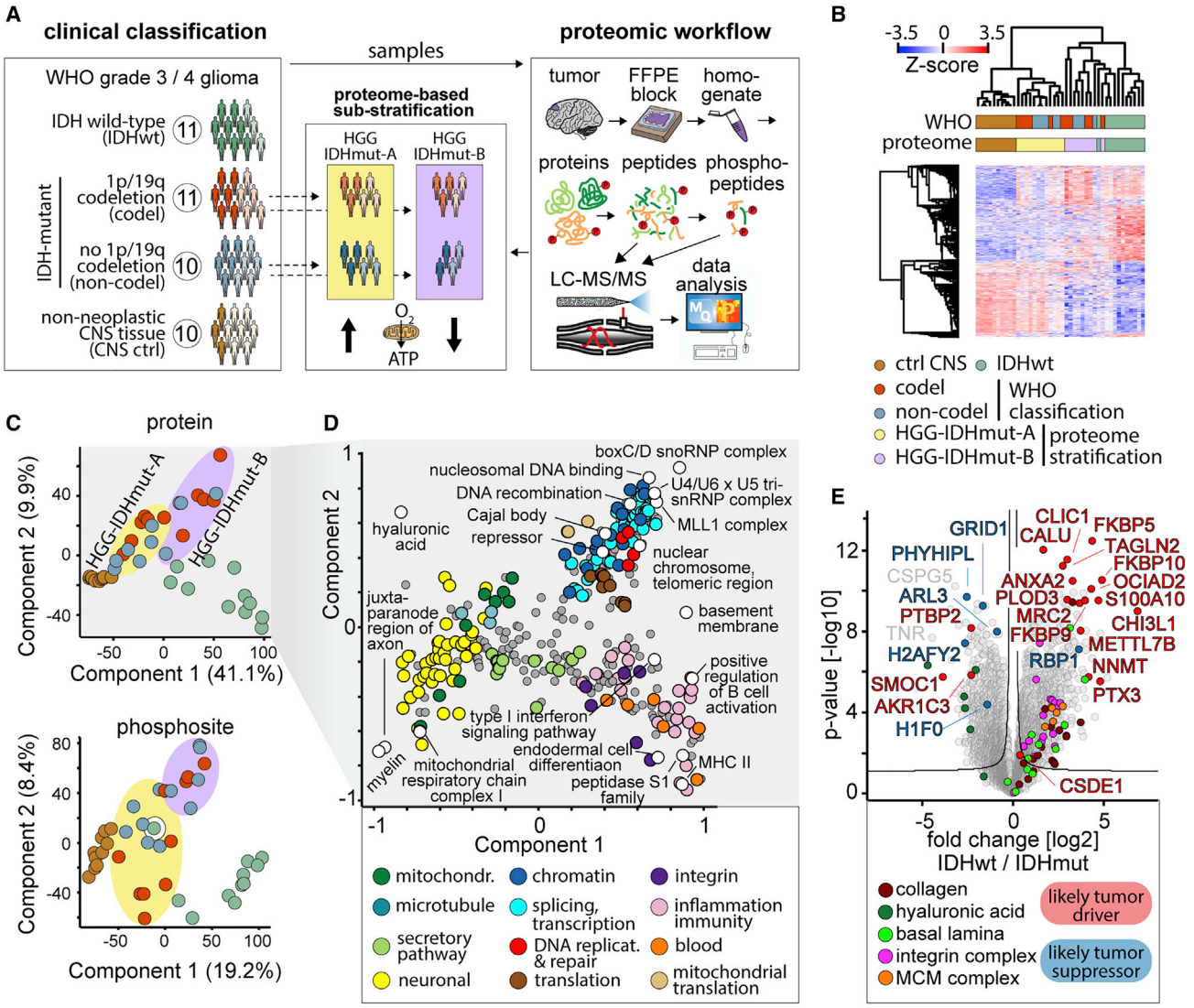

Figure 1. Study and global proteome overview

(A) Cohort overview and schematic proteomic workflow. Sample numbers in circles. Dark colors represent males and light colors females. The icons at the bottom of the proteome-based classification of IDHmut gliomas represents high (arrow up) and low (arrow down) expression levels of mitochondrial respiratory chain proteins.

(B) Unbiased hierarchical clustering of all 42 samples (columns) and proteins (rows), *Z*-scored protein intensity shown in a heatmap; 3,749 significant proteins included, significance ($q < 5\%$ at $s0 = 2$) according to one-way ANOVA analysis using the WHO-defined entities. Sample clustering based on Euclidian distance and protein clustering based on Pearson correlation.

(C) Principal-component analysis of proteomes of all 42 samples for protein abundance (upper panel) and phosphosite abundance (lower panel). Components 1 and 2 shown, respectively. Sample color code as in (A and B). Colored ellipses highlight the IDHmut HGG-IDHmut-A and HGG-IDHmut-B clusters as defined in (B).

(D) Two-dimensional analysis of protein annotation term enrichment in components 1 and 2 of the principal-component analysis of the proteome dataset linking the components to biological features.

(E) Comparison of IDHwt and IDHmut glioma proteomes. Samples, n = 11 IDHwt and 21 IDHmut.

sub-stratification with the epigenetic and CNV profile of IDH-mutated gliomas. Both IDHmut-proteome subgroups included gliomas, with astrocytoma and 1p/19q codeleted oligodendroglioma methylation subclasses at a comparable ratio ($p > 0.9$, Fisher's exact test; Table 1). Our analysis shows that CNVs did not bias these proteome groups (Figures S1H and S1I). Specifically, an evenly distributed CNV load and comparable chromosome gains or losses were found in both groups. The sub-stratification was also not imbalanced with respect to WHO grade ($p > 0.9$, Fisher's exact test; Table 1) and was statistically insignificantly imbalanced in CDKN2A/B status ($p = 0.17$, Fisher's exact test; Table 1). Furthermore, there was no imbalance in EGFR amplifications, which were only detected in IDHwt gliomas (5/11). Next, we examined whether the origin of the proteome-based sub-stratification of HGG-IDHmut-A and -B correlated with demographic patient data and histology. HGG-IDHmut-B and

Table 1. Cohort composition

	Non-neoplastic controls	Oligodendroglioma IDHmut and 1p/19q codeleted (codel)	Astrocytoma IDHmut (non-codel)	HGG-IDHmut-A	HGG-IDHmut-B	Glioblastoma (IDHwt)
N	10	11	10	12	9	11
Age at diagnosis (mean ± SD)	39 ± 12	48 ± 10	36 ± 12	38 ± 12	47 ± 12	73 ± 7
Male:female	3:7	6:5	5:5	6:6	5:4	8:3
Histopathology	parahippocampal tissue of patients with hippocampal sclerosis	11 oligodendroglioma, IDHmut and 1p/19q codeleted (CNS: WHO: 3)	10 astrocytoma, I DHmut (CNS: WHO 3/4)	6 oligodendroglioma, IDHmut and 1p/19q codeleted (CNS: WHO: 3), 6 astrocytoma, IDHmut (CNS: WHO 3/4)	5 oligodendroglioma, IDHmut and 1p/19q codeleted (CNS: WHO: 3), 4 astrocytoma, IDHmut (CNS: WHO 3/4)	11 glioblastoma, IDHwt (CNS: WHO 4)
WHO grade 3:4	Na	11:0	8:2	11:1	8:1	0:11
IDH status	Na	11 IDH1 R132H	10 IDH1 R132H	12 IDH1 R132H	9 IDH1 R132H	11 wt
1p/19q status (LOH microsatellite)	Na	11 codeletion	10 intact	6 codeletion, 6 intact	5 codeletion, 4 intact	11 intact
CDKN2A/B deletion	Na	1/11	1/10	0/12	2/9	8/11
EGFR amplification	Na	0/11	0/10	0/12	0/9	5/11
Methylation class	Na	11 methylation class family glioma, IDHmut	9 methylation class family glioma, IDHmut, 1x non-classifiable	11 methylation class family glioma, IDHmut, 1 non-classifiable	9 methylation class family glioma, IDHmut	11 methylation class family glioma, IDHwt, 1 non-classifiable
Methylation subclass	Na	10 1p/19q-codeleted oligodendroglioma, 1 oligosarcoma	8 astrocytoma, 1 high-grade astrocytoma, 1 non-classifiable	6 1p/19q codeleted oligodendroglioma, 5 astrocytoma, 1 non-classifiable	4 1p/19q codeleted oligodendroglioma, 1 oligosarcoma, 3 astrocytoma, 1 high-grade astrocytoma	4 RTK II, 3 RTK I, 3 mesenchymal, 1 non-classifiable

Table 2. Proteins of interest with differential abundance in various glioma subtypes in the proteomic data of this study

Sample group	Gene, protein	Role	Tumor entity	Cellular function	Reference
Selected outlier proteins regulated between IDHwt and IDHmut					
IDHwt	CHI3L1, chitinase-3-like protein 1	OG	glioma, breast cancer	inflammation, angiogenesis	Libreros et al.[29]; Steponaitis et al.[30]
	FKBP5/FKBP9/FKBP10, peptidyl-prolyl *cis-trans* isomerase FKBP5/9/10	OG	glioma, renal cell carcinoma	FKBP5: NF-κB signaling FKBP9: MAPK signaling FKBP10: proliferation, invasion	Jiang et al.[31]; Xu et al.[32]; Ge et al.[33]
	CALU, calumenin	OG	glioma	EMT	Yang et al.[34]
	TAGLN2, transgelin-2	OG	glioma	cell motility	Han et al.[35]
	PLOD3*	OG	glioma	proliferation, invasion, hypoxia	Tsai et al.[36]
	S100A10, protein S100-A10*	OG	glioma, various	ECM remodeling, invasion	Tantyo et al.[37]
	ANXA2, annexin A2*			prevents S100A10 degradation	
	OCIAD2, OCIA domain-containing protein 2	OG	glioma, various	migration, invasion	Nikas 2016[38]; Sinha et al.[39]
	MRC2, C-type mannose receptor 2	OG	hepatocellular carcinoma	migration, invasion, TGF-β signaling	Gai et al.[40]
	METTL7B, methyltransferase-like protein 7B	OG	lung cancer	cell-cycle progression	Liu et al.[41]
	CLIC1, chloride intracellular channel protein 1	OG	glioblastoma	proliferation	Setti et al.[42]
	PTX3, pentraxin-related protein PTX3	OG	glioblastoma	autophagy	Wang et al.[43]
	RBP1, retinol-binding protein 1	TSG	IDHmut glioma	retinoic acid metabolism	Chou et al.[44]
	CSDE1, cold-shock domain-containing protein E1	OG	colorectal cancer	differentiation, EMT	Lee et al., 2017[45]; Martinez-Useros et al.[46]
	NNMT, nicotinamide N-methyltransferase	OG	ovarian cancer	ECM	Eckert et al.[47]

(*Continued on next page*)

CellPress
OPEN ACCESS

Table 2. *Continued*

Sample group	Gene, protein	Role	Tumor entity	Cellular function	Reference
IDHmut	H1F0, histone H1.0	TSG	various, including glioblastoma	differentiation, epigenome	Torres et al.[27]
	H2AFY2, core histone macro-H2A.2	TSG	melanoma	differentiation, epigenome	Gaspar-Maia et al.[28]; Kapoor et al.[48]
	ARL3, ADP-ribosylation factor-like protein 3	TSG	glioma	not clear yet	Wang et al.[49]
	GRID1, glutamate receptor ionotropic, delta-1	NA	glioma	not clear yet	Wang et al.[50]
	PHYHIPL, phytanoyl-CoA hydroxylase interacting protein-like	TSG	glioblastoma	TNF signaling	Fu et al.[51]
	AKR1C3, aldo-keto reductase family1 member C3	OG	liver cancer, prostate cancer	metabolism EMT, ERK signaling	Zhao et al. [52]; Wang et al.[53]
	PTBP2, polypyrimidine tract-binding protein 2	OG	glioma	proliferation, migration	Cheung et al.[54]
	SMOC1, SPARC-related modular calcium-binding protein 1	NA	oligodendroglioma	ECM	Brellier et al.[55]
Selected outlier proteins regulated between I DHmut glioma subgroups					
HGG-IDHmut-B	CCAR1/2, cell division cycle and apoptosis regulator protein ½	OG, (TSG)	various	Wnt/β-catenin, DNA damage, cell-cycle, cell growth, apoptosis	Johnson et al.[56]
	YBX1, Y-box-binding protein 1	OG	various, including glioblastoma	proliferation, survival, invasion	Maurya et al. [57]; Kuwano et al.[58]; Gupta et al.[59]
	PRDX4, periredoxin-4	OG	various, including glioblastoma	oxidative stress, apoptosis	Jia et al. [60]; Kim et al.[61]
	SUPT5H, transcription elongation factor SPT5	OG	colorectal carcinoma	telomerase expression	Chen et al.[62]
	LAMB1, laminin subunit beta-1	OG	hepatocellular carcinoma	invasion	Govaere et al.[63]
	LUM, lumican	OG	lung cancer	metastasis	Hsiao et al.[64]
	ERH, enhancer of rudimentary homolog	OG	breast, ovarian, liver, and bladder urothelial cancer	splicing, cell cycle, DNA replication and repair, EMT and invasion	Graille and Rougemaille[65]; Pang et al.[66]; Zhang et al.[67]

(*Continued on next page*)

Table 2. *Continued*

Sample group	Gene, protein	Role	Tumor entity	Cellular function	Reference
1p/19q codel	RPS6K/MSK1, ribosomal protein S6 kinase alpha-5	OG	breast cancer, glioblastoma	differentiation, metastasis, drug resistance	Gawrzak et al. [68]; Wu et al.[69]
	LRP4, low-density lipoprotein receptor-related protein 4	OG	papillary thyroid cancer	proliferation, invasion	Zhou et al.[70]
	TRIM67, tripartite motif-containing protein 67	OG TSG	lung cancer, colorectal cancer	proliferation, invasion, p53 activation	Jiang et al.[71]; Wang et al.[72]
Non-1p/19q codel	FBLN1, fibulin-1	TSG	various	apoptosis, cell motility	Kanda et al. [73]; Xiao et al.[74]
	TNC, tenascin-C	OG	glioblastoma, various others	invasion, proliferation, EMT	Xia et al.[75]; Yoshida et al.[76]
UniProt annotated tumor suppressors and oncoproteins—analysis across glioma groups					
Reduced in IDHwt and HGG-IDHmut-B	DMTN, dematin	TSG	colorectal cancer	metastasis	Ye et al.[77]
	CYLD, ubiquitin carboxyl-terminal hydrolase CYLD	TSG	skin cancer, myeloma	NF-κB signaling	Sun[78]
	BIN1, Myc box-dependent-interacting protein 1	TSG	lung cancer	c-Myc signaling	Zhang et al.[79]
Reduced in IDHwt	NDRG2, protein NDRG2	TSG	lymphoma	AKT signaling	Nakahata et al.[80]
	CDKN1B/p27^{Kip1}, cyclin-dependent kinase inhibitor 1B	TSG	various	cell cycle	Bencivenga et al.[81]
	NF1, neurofibromin	TSG	glioma, various	Ras signaling	Lobbous et al.[82]
Reduced in HGG-IDHmut-B	PRKCD, protein kinase C delta type	TSG/(OG)	lymphoma, breast cancer	apoptosis, p53 signaling, ErbB2 signaling	Dashzeveg and Yoshida [83]; Baumann et al.[84]; Allen-Petersen et al.[85]
	RPS6KA2	TSG	ovarian cancer	proliferation, apoptosis	Bignone et al.[86]
High in IDHwt	PYCARD, apoptosis-associated speck-like protein a CARD	TSG/OG	glioblastoma	inflammasome	Stone et al.[87]; Sharma et al.[88]; Martinon et al.[89]
	DAB2, disabled homolog 2	TSG/other	mesenchymal glioblastoma	tumor microenvironment, inflammation	Behnan et al. [90]; Figliuolo da Paz et al.[91]
	NFKB2, NF-κB p100 subunit	(OG)	glioblastoma	mesenchymal differentiation, EMT	Yamini[92]

(*Continued on next page*)

Table 2. *Continued*

Sample group	Gene, protein	Role	Tumor entity	Cellular function	Reference
High in IDHwt and HGG-IDHmut-B	EGFR, epidermal growth factor receptor	OG	glioma	survival, proliferation, invasion	Oprita et al.[93]
	AKT2, protein kinase Akt-2	OG	glioma	metabolism, proliferation, survival	Pu et al.[94]; Kim et al.[95]
	NUP214, nuclear pore complex protein Nup214 DEK, protein DEK SET, protein SET	OG	leukemia	fusion proteins DEK-NUP214 and SET-NUP214*: NF-κB signaling	Saito et al.[96]
	TPM3, tropomyosin alpha-3 chain	OG	glioma	EMT	Tao et al.[97]
	RBM15, RNA-binding protein 15	OG	glioma	RNA methylation	Su et al.[98]

OG, oncogene; TSG, tumor suppressor gene. Sample group denotes the samples with high protein abundance. PLOD3, multifunctional procollagen lysine hydroxylase and glycosyltransferase LH3. ANXA2 and S100A10 strongly correlated (Pearson r = 0.93) in abundance across samples (all glioma and ctrl CNS of this study). Similarly, NUP214, DEK, and SET correlated well (Pearson r = 0.87 NUP214 vs. DEK, r = 0.76 NUP214 vs. SET) across samples (see Figure S5E).

HGG-IDHmut-A sample groups, however, were undistinguishable. The sample groups correlated neither with age nor gender of patients, nor was the separation attributable to a different total tumor cell content (Table 1; Figures S2A–S2E; see supplemental information). We did not detect statistically significant differences in progression-free survival between HGG-IDHmut-A and -B in our cohort comprising 21 IDHmut glioma (Figure S2F).

HGG-IDHmut-A/B differences reflect chromosomal and mitochondrial aberrations

After excluding systematic biases in our study groups, we next assessed whether previously described cancer-associated chromosomal aberrations can be detected in the proteomes of tumor samples. Detected proteins were evenly distributed across almost the entire genome (Figure 2A). Hierarchical clustering across tissue samples revealed a pattern recapitulating the global proteome clustering (Figure 2B). In accordance with the 1p/19q status, codel samples exhibited a significantly reduced abundance of 1p/19q-encoded proteins (Figure 2C). However, the HGG-IDHmut-A/B groups showed distinct chromosome arm-encoded proteomes, with a strikingly reduced abundance of proteins encoded by the mtDNA in HGG-IDHmut-B (Figures 2C and 2D). This trend was also evident for nuclear genome-encoded mitochondrial respiratory chain complex proteins; however, not for mitochondrial ribosomal proteins (Figure 2E). The 1p/19q codeletion status did not exhibit these mitochondrial aberrations (Figures 2D and 2F).

HGG-IDHmut-A/B stratification is linked to differential expression of cancer driver genes

Several known cancer drivers were enriched in HGG-IDHmut-B over HGG-IDHmut-A (Figure 2E; Table 2). The most significant outlier enriched in HGG-IDHmut-B was CCAR1, the related CCAR2 was less significantly enriched. Both proteins play complex roles in cancer, including gliomas.[56,99–101] Intriguingly, the best correlating protein to CCAR1 in our dataset was the splicing factor SRSF1 (Figure S3A). Its related protein SRSF5 promotes lung cancer via alternative splicing of CCAR1 upon high availability of glucose.[102] In our dataset, SRSF5 was stochastically quantified while SRSF1, 2, 3, 4, 6, 7, 10, and 11 were significantly enriched in HGG-IDHmut-B over HGG-IDHmut-A.

1p/19q codeletion status affects cancer-related proteins

Around 1,900 proteins differed significantly between the HGG-IDHmut-B and HGG-IDHmut-A sample groups in our dataset, whereas only about 100 proteins differed significantly between 1p/19q codel and non-codeleted IDHmut (Figures 2E and 2F). Nevertheless, several of the regulated proteins between codel and non-codel IDHmut have been linked to cancer in various contexts (Figure 2F; Table 2).

ATRX was among these differently expressed proteins and had a lower abundance in the non-codel sample group. This is in line with the frequent loss of ATRX in 1p/19q intact but not in 1p/19q codeleted gliomas as ATRX loss activates the "alternative lengthening of telomere"pathway.[103–105] In contrast, TERT promoter mutations are associated with IDHwt and ATRX expression.[106–108] TERT, the catalytic subunit of telomerase, was not covered in our dataset, but telomerase-accessory proteins were among the most highly enriched proteins among ATRX-correlating proteins (Figure S3B).

Next, we compared the regulation of proteins affected by common chromosomal alterations in gliomas (1p/19q codeletion, gain of chr. 7, loss of chr. 10; Figure 2C).[108,109] In our data, many proteins encoded on chromosome 10 and 7 were significantly regulated (10 reduced, 7 elevated) in IDHwt gliomas, and transcripts of these regulated proteins were expectedly associated with survival according to The Cancer Genome Atlas transcriptomics data (Figure S3C).[110] By contrast, proteins encoded on the 1p and particularly the 19q arm exhibited smaller and less statistically significant regulation and their transcripts did not show a clear association with survival (Figure S3D).

In summary, proteins encoded on 1p/19q were less drastically regulated compared with proteins affected by other common chromosomal alterations in glioma. Taken together, the overall glioma proteome showed only minor alterations correlating with the 1p/19q codeletion but reflected known cancer-related proteins, in particular in telomere maintenance pathways.

HGG-IDHmut-A/B stratification correlates with distinct metabolic profiles

The differential abundance of mitochondrial respiratory chain proteins between HGG-IDHmut-A and -B prompted us to investigate metabolic alterations in greater detail. Respiratory chain complex and tricarboxylic acid (TCA) cycle proteins exhibited a low abundance in IDHwt and HGG-IDHmut-B (Figures 3A, 3B, S4A, and S4B). Intriguingly, mild dysfunction of respiratory chain complex I—the lowest in HGG-IDHmut-B—can promote cancer via the generation of reactive oxygen species (ROS).[111] Notably, IDH1 was the only TCA protein with mildly elevated abundance in HGG-IDHmut-B. Conversely, the TCA protein oxoglutarate dehydrogenase L was strongly reduced, which may be linked to its tumor suppressor function.[112]

Regarding glycolysis, HGG-IDHmut-B again exhibited a protein and phosphosite profile similar to IDHwt (Figures 3C and S4C–S4E). In particular, hexokinase 1 was low abundant in HGG-IDHmut-B and IDHwt. Downregulation of hexokinase 1 promotes glycolysis and induces EMT in several human cancer cell lines and increased malignancy in a xenograft model.[113]

Likewise, the abundance of the pS39 site on the mitochondrial ATPase inhibitor ATPIF1 was low in both IDHwt and HGG-IDHmut-B compared with HGG-IDHmut-A (Figure 3D). ATPIF1 overexpression promotes a metabolic shift from oxidative phosphorylation to glycolysis in colon cancer,[114] while ATPIF1 is inhibited by S39 phosphorylation.[115]

In summary, HGG-IDHmut-B showed molecular hallmarks of increased glycolytic activity and HGG-IDHmut-A of increased oxidative phosphorylation, independent of 1p/19q codeletion.

Proteome-based sub-stratification correlates better with profiles of annotated tumor suppressors and drivers than 1p/19q codeletion

Next, we examined the profiles of annotated tumor suppressors and oncoproteins across the glioma entities. Principal-component analysis separated IDHwt, HGG-IDHmut-A, and HGG-IDHmut-B

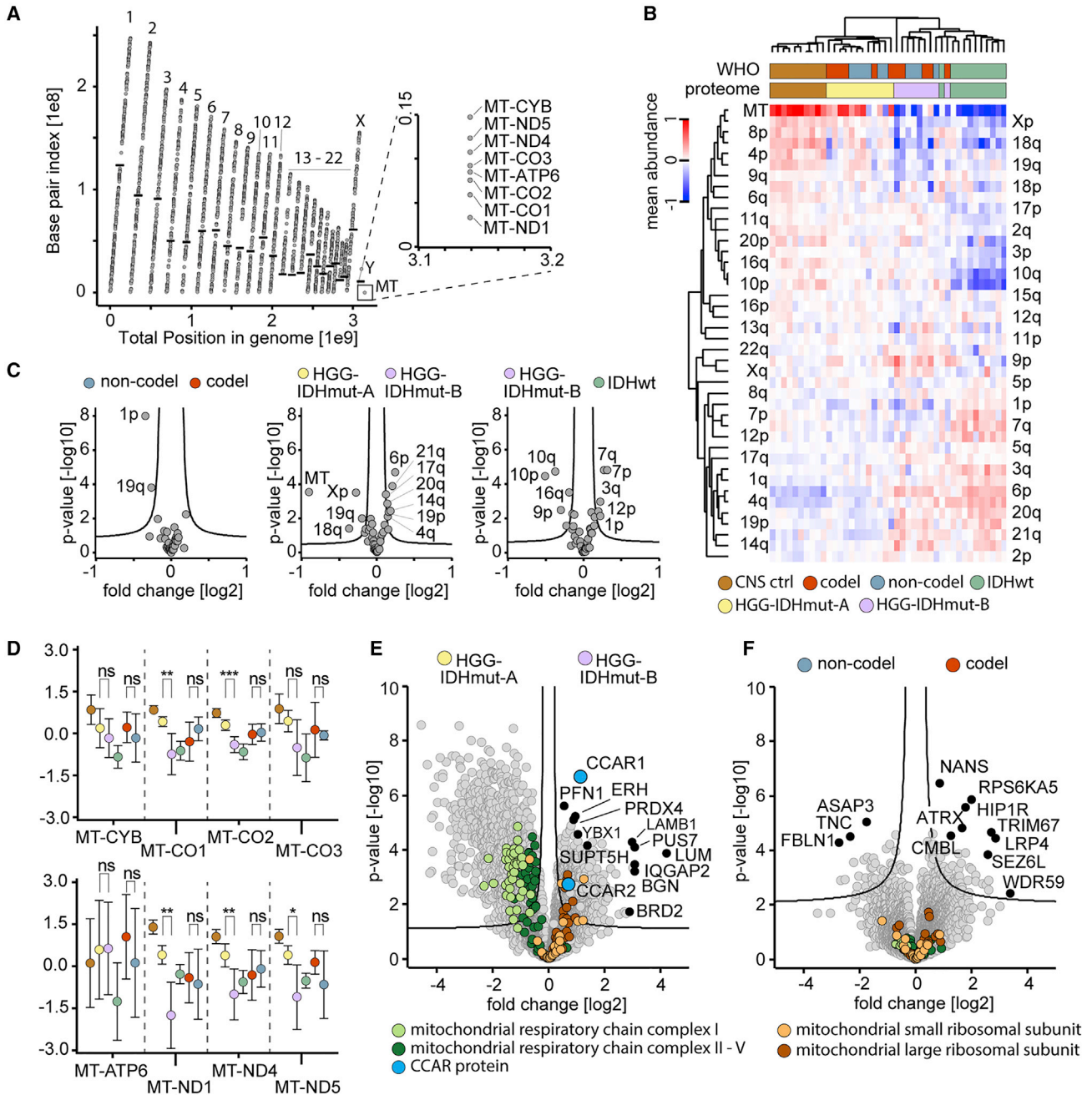

Figure 2. Chromosomal alterations point at mitochondrial perturbations in the alternatively stratified groups of IDHmut gliomas

(A) Proteome coverage across the human genome in the entire dataset (42 samples). Points indicate quantified proteins, black horizontal bars as boundaries between chromosomal p and q arms; p arms below and q arms above the bar. Uncovered areas included the p arms of chromosomes 13, 14, 15, 21, and 22, and the centromere-proximal quarter of the 9p arm.

(B) Relative abundance of chromosome arm-specific proteomes across samples shown as a heatmap. Abundance as mean intensity of all proteins assigned to a given chromosome arm. Protein intensities normalized by subtraction of median across samples before mean averaging. Samples, n = 10 (ctrl CNS), n = 12 (HGG-IDHmut-A), n = 9 (HGG-IDHmut-B), n = 11 (IDHwt), n = 11 (codel), n = 10 (non-codel).

(C) Abundance difference of chromosome arm-specific proteomes between IDHmut glioma entities. Comparison of codel (n = 11) versus non-codel entity (n = 10) (left), (center), IDHwt (n = 11) versus HGG-IDHmut-B (n = 9) (right).

(D) Abundance of proteins encoded by mitochondrial DNA across the conventional and alternatively defined tumor and control entities of this study. Circles denote means and error bars 95% confidence intervals of the mean. Color code and sample numbers as in (B).

(E and F) Global proteome and abundance differences in mitochondrial proteins between the alternative proteome-defined entities HGG-IDHmut-A (n = 12) and HGG-IDHmut-B (n = 9) (E) and the 1p/19q-codeleted (n = 11) and non-codeleted (n = 10) entities (F) of IDHmut glioma. Mitochondrial respiratory chain complex V refers to ATP synthase.

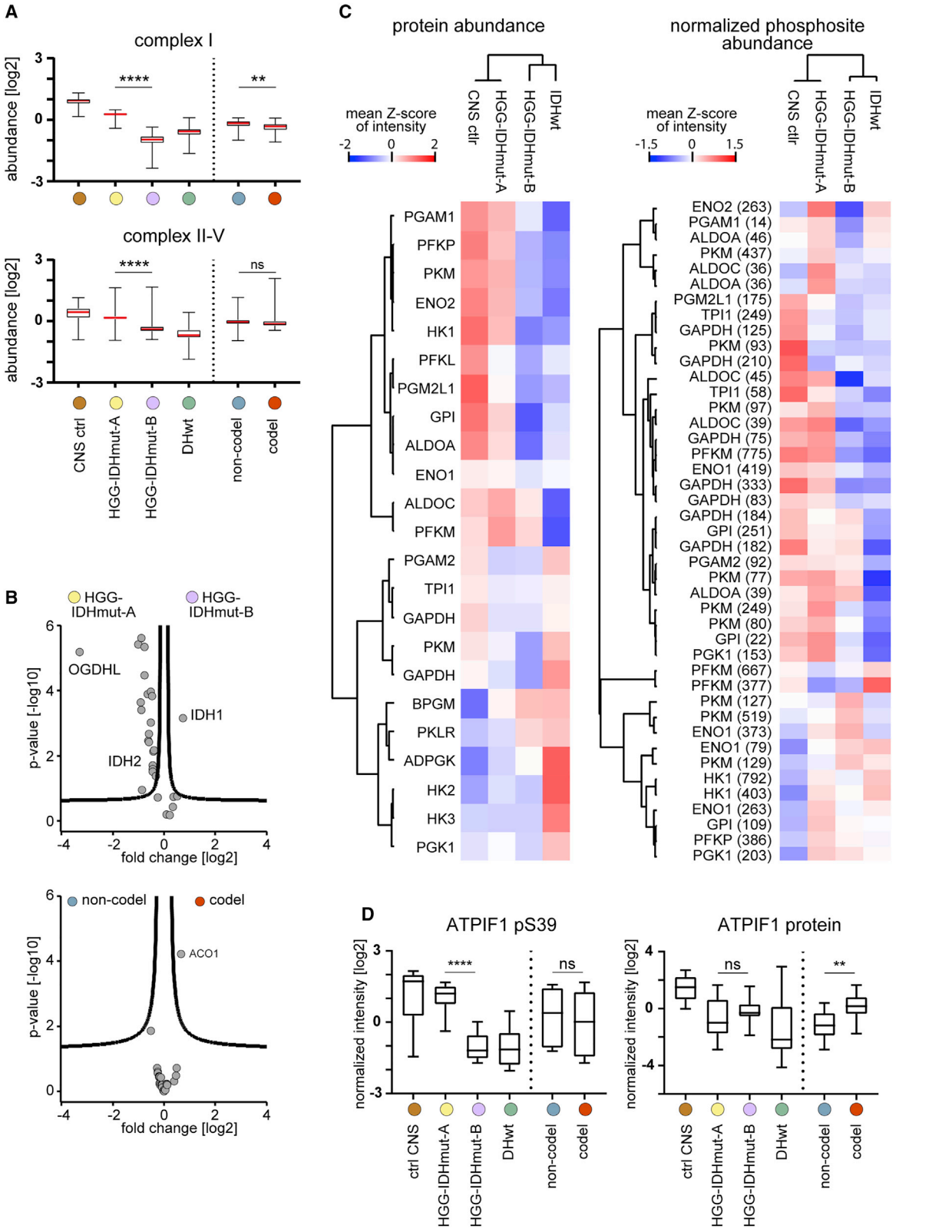

(legend on next page)

samples but not the 1p/19q codeletion status (Figures 4A, S5A, and S5B). The HGG-IDHmut-B signature was largely similar to IDHwt, while 1p/19q codeletion status was associated with few statistically significant differences (Figures 4B, S5C, and S5D).

Some tumor suppressors were specifically downregulated in IDHwt, others only in HGG-IDHmut-B, and some in both (Figure 4B; Table 2). IDHwt and HGG-IDHmut-B sample groups exhibited a downregulation of RAS pathway proteins in line with previous reports for glioblastoma (Figure 4B).[116] Conversely, several proto-oncogenes were elevated in IDHwt and HGG-IDHmut-B (Figures 4B and S5E; Table 2). For some regulated proteins, the function in the context of tumorigenesis is unclear or context dependent (Table 2).

HGG-IDHmut-B and HGG-IDHmut-A exhibited strong alterations of tumor suppressors and oncoprotein phosphosite abundances, not associated with 1p/19q codeletion status (Figures 4C and S6A–S6D). For instance, the pT595 site on the cyclin-dependent kinase CDK11B was abundant in both HGG-IDHmut-B and IDHwt compared with HGG-IDHmut-A independent of total protein levels (Figures 4C and S6C). This suggests elevated CDK11B activity due to homology with the activating pT161 site in CDK1,[117] linked to cell-cycle progression and altered in various cancers.[118] This highlights HGG-IDHmut-A and HGG-IDHmut-B signaling differences vital to cancer.

HGG-IDHmut-A/B differences are evident across studies

To validate major molecular hallmarks supporting a metabolic stratification of IDHmut gliomas independent of 1p/19q status, we reanalyzed three recent proteomics datasets. In one study dataset comprising predominantly IDHmut glioma we identified equivalent IDHmut-A and IDHmut-B subtypes using unbiased hierarchical clustering as in our dataset (Figures S7A and S7B).[119] Notably, a small number of samples in that dataset indicate that IDHmut-A/B are also present in WHO grade 2 gliomas and that proteome differences between these are equivalent to those of WHO grade 3 gliomas (Figure S7B). A second study described a similar metabolism-linked proteomic stratification of IDHwt gliomas into a glycolysis and an oxidative phosphorylation subgroup.[120] To further validate such a stratification in a larger and multi-omics glioma dataset we integrated a third study, which also comprised predominantly IDHwt gliomas.[25]

Highly consistent with our study, metabolic proteins involved in glycolysis, TCA cycle, oxidative phosphorylation, and even the global proteome were regulated in great quantitative agreement in the three other studies (Figures 5A–5D and S7C–S7F). Among the metabolic classes, TCA cycle proteins showed the most consistent and quantitatively concordant regulation across studies.

In the multi-omics dataset, our HGG-IDHmut-A (oxidative phosphorylation high) glioma subgroup corresponded to the proneural-like (nmf1) subgroup (Figure 5A). Our HGG-IDHmut-B (oxidative phosphorylation low) subgroup correlated most strongly with the classical-like (nmf3) glioma subgroup, but also considerably with the mesenchymal-like (nmf2) subgroup (Figures 5A and S7C).

In addition to metabolic changes, similarities across studies extended to other biological pathways, such as mRNA splicing, RNA metabolism, translation, chromatin dynamics, DNA replication, and a collagen-rich ECM, which were enriched in HGG-IDHmut-B and corresponding subgroups across studies (Figures S7G and S7H). Conversely, neural phenotype and mitochondrial proteins were enriched in HGG-IDHmut-A/proneural-like subgroups. Moreover, top outliers and likely cancer drivers CCAR1, YBX1, and ERH enriched in HGG-IDHmut-B were likewise regulated in other datasets (Figures 5A and S7G; Table 2).

Altogether, we show that IDHmut gliomas can be stratified into two proteomic subtypes with diverging energy metabolism and overall stronger differences than those caused by 1p/19q codeletion. Intriguingly, this separation emerges in four independent studies, not only independent of 1p/19q but also across IDHmut status.

DISCUSSION

Classification of CNS tumors has long been based on histology only. In recent years, new molecular methods have significantly improved the diagnosis of diffuse glioma and risk stratification of certain glioma subgroups. At the genetic and epigenetic level, we now know numerous driver mutations and epigenetic profiles that provide information about the emergence of these malignant tumors.

Unfortunately, these successes are not significantly reflected in the treatment of diffuse high-grade adult gliomas. As a rule, adult malignant gliomas have been treated the same way for more than 15 years, mostly independent of the molecular profile, according to the generally applicable STUPP and CATNON regimen with concomitant radiochemotherapy with 6 or 12 cycles of the alkylating agent temozolomide.[121,122] A major breakthrough in improving survival, as in other malignancies, such as breast cancer, lung cancer, or colorectal carcinomas, could not be achieved by these therapies. A targeted therapy tailored to the molecular profile, e.g., IDHmut or IDHmut and 1p/19q codeleted gliomas could not be established so far.

Therefore, we hypothesized that, in addition to the known histological-molecular tumor classification (according to the current WHO classification), a proteome-based approach could reveal

Figure 3. Metabolism-related proteome differences associated with the novel classification of IDHmut tumors

(A) Abundance of mitochondrial respiratory chain complex proteins across the sample entities of this study, split by complex I (upper panel) and complex II-V (lower panel). Samples, n = 10 (ctrl CNS), n = 12 (HGG-IDHmut-A), n = 9 (HGG-IDHmut-B), n = 11 (IDHwt), n = 11 (codel), n = 10 (non-codel).

(B) Regulation of tricarboxylic acid protein abundances between HGG-IDHmut-B and HGG-IDHmut-A entities (upper panel) but not between codeletion-defined entities (lower panel). Sample numbers as in (A).

(C) Glycolysis-related protein profiles (left panel) and protein abundance-normalized phosphosite profiles (right panel) across the proteome-defined entities. Abundances as sample group means of cross-sample *Z* scores of protein intensities and relative protein-normalized phosphosite intensities. Sample numbers as in (A).

(D) Abundance of the ATPIF1 pS39 phosphosite (left panel) and the protein abundance (right panel) across the entities of this study. Sample numbers as in (A).

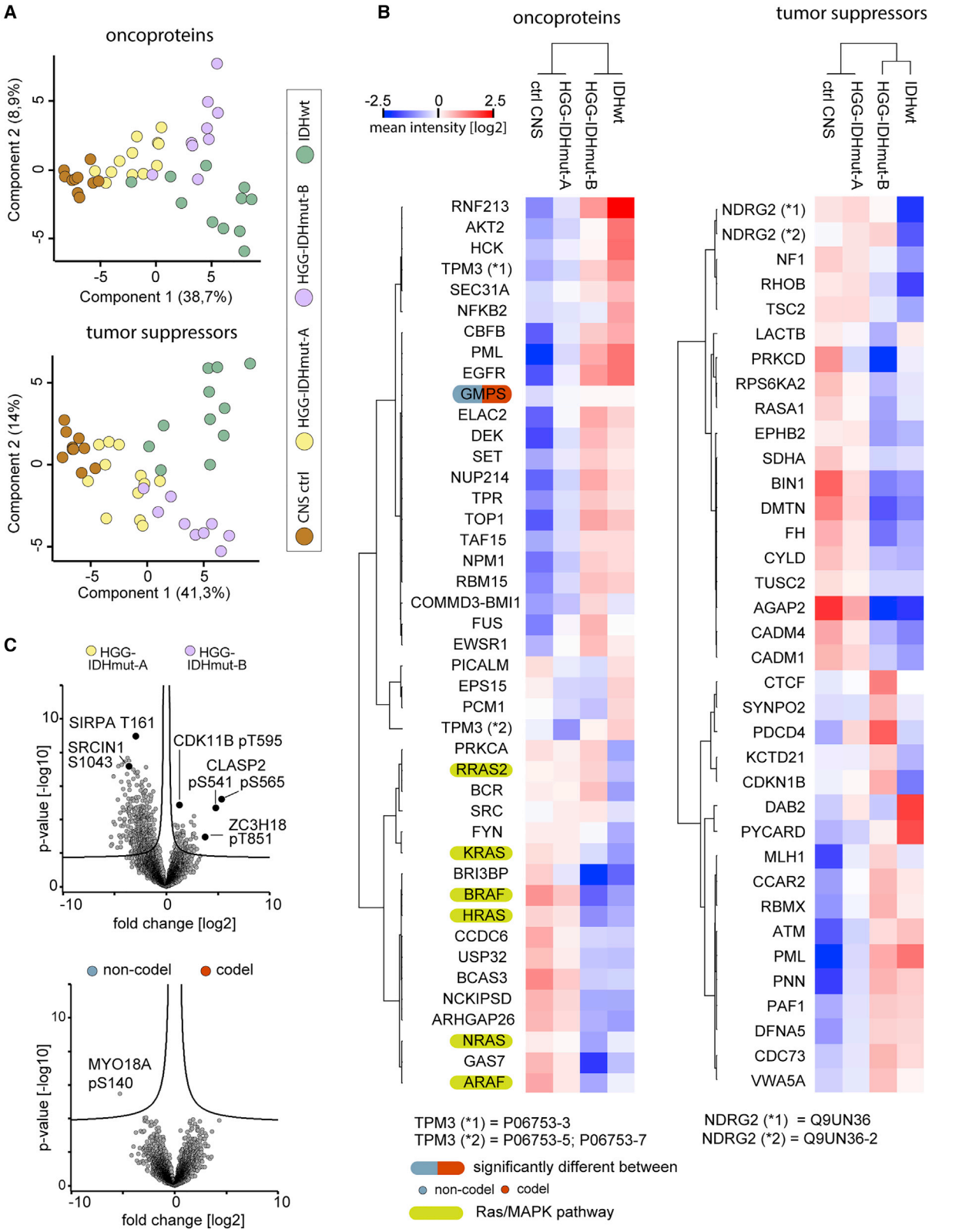

(legend on next page)

signaling pathways and metabolic states which pave the way for novel therapeutic strategies.

For this purpose, we characterized the proteome and phospho-proteome of adult-type diffuse high-grade (WHO grades 3 and 4) gliomas from FFPE samples with MS. The genetic subtyping of IDHmut tumors into astrocytoma, IDHmut and oligodendroglioma, IDHmut and 1p/19q codeleted according to the current WHO classification correlated with minor differences in the tumor proteome (WHO Classification of Central Nervous System Tumours, fifth edition). The selective loss of proteins encoded on chromosomal locations 1p and 19q was reflected in the proteomes, albeit to a lower extent than loss of chromosome 10 proteins in IDHwt gliomas. Likewise, the proteomic data showed the expected relationship of 1p/19q codeletion and molecular signatures of telomere maintenance via either the alternative lengthening of telomeres pathway or the telomerase-dependent pathway. These signatures include loss of ATRX in 1p/19q intact gliomas and conversely high abundance of telomerase-associated proteins in ATRX intact (1p/19q codeleted) gliomas. Overall, the proteomics approach discovered expected features associated with the 1p/19q codeletion.

However, the proteomes suggested an alternative sub-stratification of IDHmut gliomas independent of 1p/19q codeletion. This sub-stratification correlated with the loss of mitochondrial DNA-encoded proteins, a loss of mitochondrial respiratory chain proteins, an overall distinct metabolic profile, a basement membrane-like ECM signature, distinct proto-oncogene and tumor suppressor protein signatures, differences in translation, RNA metabolism, DNA replication, and chromatin dynamics, as well as site-specific differences in the phospho-proteomes. In this study cohort, the alternative sub-stratification was not associated with patient gender, age, clinical course, discerning histopathological features, or CNV alterations.

Occurrence of an early 1p/19q codeletion can be a crucial point in cancer development, while both codeleted and non-codeleted gliomas can progress by similar mechanisms. Accordingly, our proteome-based classification does not question the general relevance of the 1p/19q codeletion as an early-event determinant of glioma development. However, in contrast to the more dynamic proteome, 1p/19q status may not be the most appropriate marker for the current state in subsequent cancer progression.

The tumor proteomes in this study showed perturbations of various biological processes, in particular the aerobic/anaerobic energy metabolism. The downregulation of the mitochondrial respiratory chain proteins in the proteomically defined HGG-IDHmut-B subgroup could reflect the Warburg effect, which favors the anaerobic over aerobic metabolism in cancer cells. Notably, complex I was particularly affected. A mild dysfunction of complex I can promote tumor progression via ROS-dependent activation of AKT signaling.[111] Moreover, loss of respiratory chain proteins in our dataset was accompanied by a synergistic loss of pS39 phosphorylation on ATPIF1, a rewiring of the TCA cycle and glycolysis enzyme profile, including the loss of HK1, which promotes glycolysis and malignancy in mouse xenograft models.[113] Loss of S39 phosphorylation on ATPIF1 promotes a metabolic shift from oxidative phosphorylation to glycolysis and further proliferation and cell death resistance via mitochondrial ROS production in hypoxia and cancer.[114,115] Intriguingly, there could also be a link between the metabolic rewiring and CCAR1 dysregulation. In lung cancer, elevated glucose concentrations induce the splicing factor SRSF5 to promote cancer progression via alternative splicing of CCAR1.[102] In our dataset, CCAR1 was the top outlier in gliomas with respiratory chain loss and CCAR1's best correlating protein was the related SRSF1. Overall, our study provides a rich protein and phosphosite resource supporting future mechanism of action and target discovery investigations.

There is increasing evidence in the literature that high-grade gliomas show distinct metabolic subtypes, using glycolysis (Warburg effect) or oxidative phosphorylation as primary energy source.[120,123] The proteome differences between HGG-IDHmut-A and -B of our study were strikingly similar to differences of corresponding subtypes we likewise identified in another dataset of IDHmut glioma using unbiased hierarchical clustering.[119] Notably, these similarities extended to independently defined IDHwt subtypes in two more studies, both in terms of the global proteome and metabolic classes of proteins, including glycolysis, TCA cycle, and oxidative phosphorylation.[25,120]

The IDHwt dataset originating from the CPTAC multi-omic glioma study revealed that HGG-IDHmut-A (high oxidative phosphorylation) of our study corresponded to a proneural-like glioma subtype and HGG-IDHmut-B (low oxidative phosphorylation) corresponded best to a classical but also relatively well to a mesenchymal-like glioma subtype.[25] Thus, the HGG-IDHmut-B group in our cohort potentially comprises both mesenchymal and classic phenotype-like IDHmut glioma, which have common strong proteome differences to proneural-like IDHmut glioma.

The strong similarity of the proteome differences between IDHmut subtypes in our study, compared with the differences between IDHwt subtypes in the two other studies emerging from our analysis, suggests a shared—but yet to be determined—molecular mechanism for this phenotypic, including metabolic divergence across IDH status. Single-cell transcriptome analysis

Figure 4. The alternative sub-stratification of IDHmut gliomas correlates with altered tumor suppressor, onco-proteins, and phosphosite levels

(A) Principal-component analysis of UniProt keyword-annotated proto-oncogenes (upper panel) and tumor suppressor genes (lower panel). Samples, n = 10 (ctrl CNS), n = 12 (HGG-IDHmut-A), n = 9 (HGG-IDHmut-B), n = 11 (IDHwt).

(B) Abundance profiles of oncoprotein (left) and tumor suppressor (right) proteins across the proteomic entities of this study. Protein intensities are first normalized by subtraction of cross-sample median and then averaged by mean sample group abundance. Samples, n = 12 (HGG-IDHmut-A), n = 9 (HGG-IDHmut-B), n = 11 (codel), n = 10 (non-codel).

(C) Phosphosite abundance differences between the proteomic entities of this study (upper panel) and the 1p/19q codeletion-defined entities (lower panel). Sample numbers as in (A).

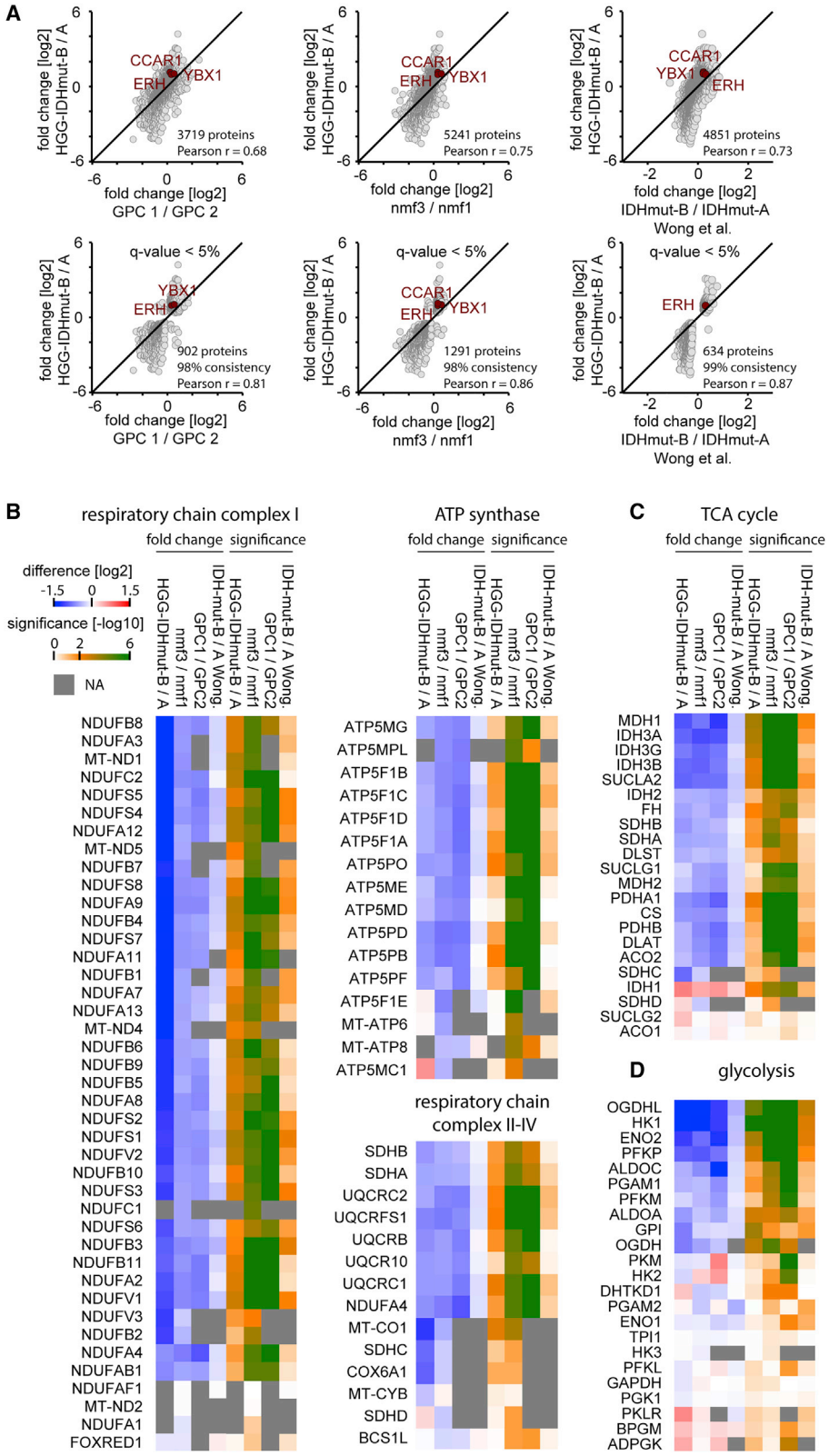

(legend on next page)

of gliomas has revealed that tumors comprise cells of four phenotypic subtypes with distinct metabolism in varying overall compositions.[123] Intrinsic (e.g., genetic/epigenetic) factors may cause such diversity and extrinsic factors (e.g., tumor microenvironment) could select for a certain cellular or overall tumor type. Further studies based on single-cell characterization, such as by emerging proteomics approaches, will be valuable in addressing these questions by defining the metabolic and neurodevelopmental tumor cell states and their microenvironment.[124]

Metabolic stratification of gliomas is an emerging approach with broad implications for survival and therapy. Re-analysis of The Cancer Genome Atlas cohort comprising over 300 human IDHwt glioblastoma samples using a pathway-based classification of the transcriptome showed a better survival of oxidative phosphorylation-driven gliomas.[123] Patient-derived cells originating from tumors relying on oxidative phosphorylation were uniquely susceptible to compounds targeting mitochondria, including inhibition of respiratory chain complex I (metformin), inhibition of mitochondrial translation (tigecycline), and induction of mitochondrial oxidative stress and apoptosis (menadione). Likewise, these cells also exhibited increased sensitivity to ionizing radiation, which primarily causes mitochondrial rather than nuclear stress.[123,125] Similarly, another study screened anticancer agents for efficacy in patient-derived cells originating from IDHwt gliomas with proteomically characterized metabolic state.[120] Several agents were selectively cytotoxic in either glycolysis-reliant glioma cells (tandutinib, crizotinib, olaparib, and AZD2014) or in oxidative phosphorylation-reliant cells (erismodegib and canertinib). Moreover, the proteomic/metabolic stratification of IDHmut gliomas may be relevant for treatment with other established drugs. For instance, IDH1 was selectively more abundant in HGG-IDHmut-B than in HGG-IDHmut-A despite the opposite trend for all other regulated TCA cycle proteins, which may correspond to differential sensitivity toward IDH inhibitors, such as ivosidenib, and a benefit in clinical trials.[126,127] Similarly, metformin is under discussion as a glioma drug, potentially in synergistic use with temozolomide, and has shown differential efficacy in cellular models of patient-derived cells derived from proteomic-metabolically stratified gliomas.[123,128,129] In summary, past studies highlight the promise that metabolic stratification holds for glioma precision medicine and as well as the power of proteomics in discovering such stratification exemplified for IDHwt glioma. By further implicating IDHmut gliomas, our study creates a bigger picture of common phenotypic subtypes independent of the IDH status, which we believe will also benefit patients with IDHmut gliomas by making future proteome/metabolism-directed therapies available to them as well.

Limitations of the study

A limitation of this study is the low number of IDHmut samples (21 IDHmut tissue samples in total). Validation in the three literature datasets provided additional support. Samples in two of the three studies were predominantly IDHwt, but in the third predominantly IDHmut. We conclude that IDHmut gliomas can be classified into metabolic and proteomic subgroups similar to those of IDHwt. However, this study does not ascertain whether proteomic/metabolic status and IDH mutational status are independent and orthogonal classifiers of a continuum of glioma phenotypes. Alternatively, similar metabolic glioma subgroups could exist within both IDHwt and IDHmut. Furthermore, the mechanistic root cause driving subtype divergence and its interplay with the (epi-)genome and tumor microenvironment remains to be elucidated.

On the clinical side, larger and clinically better-characterized study collectives are required to integrate the novel proteomic/metabolic subgroups and the established IDH mutation and 1p/19q codeletion status into a new overall classification scheme and assess the predictive power of these features for survival and treatment response. Moreover, prospective studies are required to assess whether patients with high-grade gliomas benefit from a combination of metabolic/proteomic stratification and precision anticancer agents and radiotherapy.

STAR★METHODS

Detailed methods are provided in the online version of this paper and include the following:

- KEY RESOURCES TABLE
- RESOURCE AVAILABILITY
  - Lead contact
  - Materials availability
  - Data and code availability
- EXPERIMENTAL MODEL AND SUBJECT DETAILS
  - Human subjects
- METHOD DETAILS
  - Clinical diagnostic procedures and sampling
  - DNA methylation and copy number variation analysis
  - Sample preparation for mass spectrometry
  - Ultra-high pressure liquid chromatography and mass spectrometry
- QUANTIFICATION AND STATISTICAL ANALYSIS
  - DNA methylation and copy number variation data analysis
  - Progression-free survival analysis
  - Mass spectrometry data processing
  - Data preprocessing and bioinformatic analysis

Figure 5. Comparison of HGG-IDHmut-B/HGG-IDHmut-A to the proteomic data of three other glioma studies

HGG-IDHmut-A (n = 12) and HGG-IDHmut-B (n = 9) correlate with the high and low oxidative phosphorylation glioma subgroups reported as GPC2 (n = 13) and GPC1 (n = 26),[120] nmf1/proneural-like (n = 29) and nmf3/classical-like (n = 25),[25] and IDHmut-A (n = 10) and IDHmut-B (n = 28),[119] respectively.

(A) Pairwise comparison of fold changes across all proteins overlapping in both datasets (upper panel) and across all proteins significantly regulated ($q < 5\%$) in both datasets.

(B) Regulation of mitochondrial respiratory chain proteins across datasets.

(C) Regulation of tricarboxylic acid cycle proteins across datasets.

(D) Regulation of glycolysis proteins across datasets.

- Phosphoproteome-specific analysis
- Proteome annotations, chromosomal analysis, and survival associations
- Tumor content analyses
- Integration with other glioma proteome datasets

SUPPLEMENTAL INFORMATION

Supplemental information can be found online at https://doi.org/10.1016/j.xcrm.2022.100877.

ACKNOWLEDGMENTS

We thank Igor Paron for technical assistance and Fabian Coscia for advice regarding the proteomic workflow, as well as Elis Perez and Amos Münch for the evaluation of the CNV data and statistical analyses. Funding was provided by the Max Planck Society for the Advancement of Science and the German Research Foundation DFG under project IDs 360372040 (SFB 1335), 408885537 (TRR 274), and 390873048 (EXC 2151 ImmunoSensation2).

AUTHOR CONTRIBUTIONS

J.M.B. prepared the samples for MS, acquired and analyzed mass spectrometric data, generated figures, and drafted the manuscript. J.M.B. and F.M. analysed and interpreted data. N.D., M. Misch, and A.K. selected and analyzed the samples histopathologically and interpreted the data. A.K. performed the CNV and EPIC analyses, analyzed the data, and generated figures. F.M., N.D., and M. Mann conceived and guided the study. F.M., N.D., and A.K. edited the manuscript.

DECLARATION OF INTERESTS

The authors declare no competing interests.

Received: August 25, 2021
Revised: July 15, 2022
Accepted: December 7, 2022
Published: December 29, 2022

SUPPORTING CITATIONS

The following reference appears in the Supplemental Information: [145–160].

REFERENCES

1. Ostrom, Q.T., Bauchet, L., Davis, F.G., Deltour, I., Fisher, J.L., Langer, C.E., Pekmezci, M., Schwartzbaum, J.A., Turner, M.C., Walsh, K.M., et al. (2014). The epidemiology of glioma in adults: a state of the science review. Neuro Oncol. *16*, 896–913. https://doi.org/10.1093/neuonc/nou087.
2. WHO Classification of Tumours Editorial Board (2021). World Health Organization Classification of Tumours of the Central Nervous System, 5th ed (International Agency for Research on Cancer).
3. Dolecek, T.A., Propp, J.M., Stroup, N.E., and Kruchko, C. (2012). CBTRUS statistical report: primary brain and central nervous system tumors diagnosed in the United States in 2005-2009. Neuro Oncol. *14*, v1–v49. https://doi.org/10.1093/neuonc/nos218.
4. Stupp, R., Hegi, M.E., Mason, W.P., van den Bent, M.J., Taphoorn, M.J.B., Janzer, R.C., Ludwin, S.K., Allgeier, A., Fisher, B., Belanger, K., et al. (2009). Effects of radiotherapy with concomitant and adjuvant temozolomide versus radiotherapy alone on survival in glioblastoma in a randomised phase III study: 5-year analysis of the EORTC-NCIC trial. Lancet Oncol. *10*, 459–466. https://doi.org/10.1016/S1470-2045(09)70025-7.
5. Ohgaki, H., and Kleihues, P. (2007). Genetic pathways to primary and secondary glioblastoma. Am. J. Pathol. *170*, 1445–1453. https://doi.org/10.2353/ajpath.2007.070011.
6. Yan, H., Parsons, D.W., Jin, G., McLendon, R., Rasheed, B.A., Yuan, W., Kos, I., Batinic-Haberle, I., Jones, S., Riggins, G.J., et al. (2009). Mutations in gliomas. N. Engl. J. Med. *360*, 765–773.
7. Hu, N., Richards, R., and Jensen, R. (2016). Role of chromosomal 1p/19q co-deletion on the prognosis of oligodendrogliomas: a systematic review and meta-analysis. Interdiscip. Neurosurg. *5*, 58–63. https://doi.org/10.1016/j.inat.2016.06.008.
8. Chen, J., McKay, R.M., and Parada, L.F. (2012). Malignant glioma: lessons from genomics, mouse models, and stem cells. Cell *149*, 36–47. https://doi.org/10.1016/j.cell.2012.03.009.
9. Jenkins, R.B., Blair, H., Ballman, K.V., Giannini, C., Arusell, R.M., Law, M., Flynn, H., Passe, S., Felten, S., Brown, P.D., et al. (2006). A t(1;19)(q10;p10) mediates the combined deletions of 1p and 19q and predicts a better prognosis of patients with oligodendroglioma. Cancer Res. *66*, 9852–9861. https://doi.org/10.1158/0008-5472.CAN-06-1796.
10. Leeper, H.E., Caron, A.A., Decker, P.A., Jenkins, R.B., Lachance, D.H., and Giannini, C. (2015). IDH mutation, 1p19q codeletion and ATRX loss in WHO grade II gliomas. Oncotarget *6*, 30295–30305. https://doi.org/10.18632/oncotarget.4497.
11. Riddick, G., and Fine, H.A. (2011). Integration and analysis of genome-scale data from gliomas. Nat. Rev. Neurol. *7*, 439–450. https://doi.org/10.1038/nrneurol.2011.100.
12. Lin, N., Yan, W., Gao, K., Wang, Y., Zhang, J., and You, Y. (2014). Prevalence and clinicopathologic characteristics of the molecular subtypes in malignant glioma: a multi-institutional analysis of 941 cases. PLoS One *9*, e94871. https://doi.org/10.1371/journal.pone.0094871.
13. Ceccarelli, M., Barthel, F.P., Malta, T.M., Sabedot, T.S., Salama, S.R., Murray, B.A., Morozova, O., Newton, Y., Radenbaugh, A., Pagnotta, S.M., et al. (2016). Molecular profiling reveals biologically discrete subsets and pathways of progression in diffuse glioma. Cell *164*, 550–563. https://doi.org/10.1016/j.cell.2015.12.028.
14. Capper, D., Jones, D.T.W., Sill, M., Hovestadt, V., Schrimpf, D., Sturm, D., Koelsche, C., Sahm, F., Chavez, L., Reuss, D.E., et al. (2018). DNA methylation-based classification of central nervous system tumours. Nature *555*, 469–474. https://doi.org/10.1038/nature26000.
15. Shirahata, M., Ono, T., Stichel, D., Schrimpf, D., Reuss, D.E., Sahm, F., Koelsche, C., Wefers, A., Reinhardt, A., Huang, K., et al. (2018). Novel, improved grading system(S) for IDH-mutant astrocytic gliomas. Acta Neuropathol. *136*, 153–166. https://doi.org/10.1007/s00401-018-1849-4.
16. Aebersold, R., and Mann, M. (2016). Mass-spectrometric exploration of proteome structure and function. Nature *537*, 347–355. https://doi.org/10.1038/nature19949.
17. Coscia, F., Lengyel, E., Duraiswamy, J., Ashcroft, B., Bassani-Sternberg, M., Wierer, M., Johnson, A., Wroblewski, K., Montag, A., Yamada, S.D., et al. (2018). Multi-level proteomics identifies CT45 as a chemosensitivity mediator and immunotherapy target in ovarian cancer. Cell *175*, 159–170.e16. https://doi.org/10.1016/j.cell.2018.08.065.
18. Coscia, F., Doll, S., Bech, J.M., Schweizer, L., Mund, A., Lengyel, E., Lindebjerg, J., Madsen, G.I., Moreira, J.M., and Mann, M. (2020). A streamlined mass spectrometry–based proteomics workflow for large-scale FFPE tissue analysis. J. Pathol. *251*, 100–112. https://doi.org/10.1002/path.5420.
19. Kohale, I.N., Burgenske, D.M., Mladek, A.C., Bakken, K.K., Kuang, J., Boughey, J.C., Wang, L., Carter, J.M., Haura, E.B., Goetz, M.P., et al. (2021). Quantitative analysis of tyrosine phosphorylation from FFPE tissues reveals patient-specific signaling networks. Cancer Res. *81*, 3930–3941. https://doi.org/10.1158/0008-5472.CAN-21-0214.
20. Wakabayashi, M., Yoshihara, H., Masuda, T., Tsukahara, M., Sugiyama, N., and Ishihama, Y. (2014). Phosphoproteome analysis of formalin-fixed

and paraffin-embedded tissue sections mounted on microscope slides. J. Proteome Res. *13*, 915–924. https://doi.org/10.1021/pr400960r.

21. Friedrich, C., Schallenberg, S., Kirchner, M., Ziehm, M., Niquet, S., Haji, M., Beier, C., Neudecker, J., Klauschen, F., and Mertins, P. (2021). Comprehensive micro-scaled proteome and phosphoproteome characterization of archived retrospective cancer repositories. Nat. Commun. *12*, 3576. https://doi.org/10.1038/s41467-021-23855-w.
22. Johansson, H.J., Socciarelli, F., Vacanti, N.M., Haugen, M.H., Zhu, Y., Siavelis, I., Fernandez-Woodbridge, A., Aure, M.R., Sennblad, B., Vesterlund, M., et al. (2019). Breast cancer quantitative proteome and proteogenomic landscape. Nat. Commun. *10*, 1600–1614. https://doi.org/10.1038/s41467-019-09018-y.
23. Bouchal, P., Schubert, O.T., Faktor, J., Capkova, L., Imrichova, H., Zoufalova, K., Paralova, V., Hrstka, R., Liu, Y., Ebhardt, H.A., et al. (2019). Breast cancer classification based on proteotypes obtained by SWATH mass spectrometry. Cell Rep. *28*, 832–843.e7. https://doi.org/10.1016/j.celrep.2019.06.046.
24. Zagorac, I., Fernandez-Gaitero, S., Penning, R., Post, H., Bueno, M.J., Mouron, S., Manso, L., Morente, M.M., Alonso, S., Serra, V., et al. (2018). In vivo phosphoproteomics reveals kinase activity profiles that predict treatment outcome in triple-negative breast cancer. Nat. Commun. *9*, 3501. https://doi.org/10.1038/s41467-018-05742-z.
25. Wang, L.-B., Karpova, A., Gritsenko, M.A., Kyle, J.E., Cao, S., Li, Y., Rykunov, D., Colaprico, A., Rothstein, J.H., Hong, R., et al. (2021). Proteogenomic and metabolomic characterization of human glioblastoma. Cancer Cell *39*, 509–528.e20. https://doi.org/10.1016/j.ccell.2021.01.006.
26. Sim, H., Hu, B., and Viapiano, M.S. (2009). Reduced expression of the hyaluronan and proteoglycan link proteins in malignant gliomas. J. Biol. Chem. *284*, 26547–26556. https://doi.org/10.1074/jbc.M109.013185.
27. Torres, C.M., Biran, A., Burney, M.J., Patel, H., Henser-Brownhill, T., Cohen, A.H.S., Li, Y., Ben-Hamo, R., Nye, E., Spencer-Dene, B., et al. (2016). The linker histone H1.0 generates epigenetic and functional intratumor heterogeneity. Science *353*, aaf1644. https://doi.org/10.1126/science.aaf1644.
28. Gaspar-Maia, A., Qadeer, Z.A., Hasson, D., Ratnakumar, K., Leu, N.A., Leroy, G., Liu, S., Costanzi, C., Valle-Garcia, D., Schaniel, C., et al. (2013). MacroH2A histone variants act as a barrier upon reprogramming towards pluripotency. Nat. Commun. *4*, 1565. https://doi.org/10.1038/ncomms2582.
29. Libreros, S., Garcia-Areas, R., and Iragavarapu-Charyulu, V. (2013). CHI3L1 plays a role in cancer through enhanced production of pro-inflammatory/pro-tumorigenic and angiogenic factors. Immunol. Res. *57*, 99–105. https://doi.org/10.1007/s12026-013-8459-y.
30. Steponaitis, G., Skiriutė, D., Kazlauskas, A., Golubickaitė, I., Stakaitis, R., Tamašauskas, A., and Vaitkienė, P. (2016). High CHI3L1 expression is associated with glioma patient survival. Diagn. Pathol. *11*, 42. https://doi.org/10.1186/s13000-016-0492-4.
31. Jiang, W., Cazacu, S., Xiang, C., Zenklusen, J.C., Fine, H.A., Berens, M., Armstrong, B., Brodie, C., and Mikkelsen, T. (2008). FK506 binding protein mediates glioma cell growth and sensitivity to rapamycin treatment by regulating NF-κB signaling pathway. Neoplasia *10*, 235–243. https://doi.org/10.1593/neo.07929.
32. Xu, H., Liu, P., Yan, Y., Fang, K., Liang, D., Hou, X., Zhang, X., Wu, S., Ma, J., Wang, R., et al. (2020). FKBP9 promotes the malignant behavior of glioblastoma cells and confers resistance to endoplasmic reticulum stress inducers. J. Exp. Clin. Cancer Res. *39*, 44. https://doi.org/10.1186/s13046-020-1541-0.
33. Ge, Y., Xu, A., Zhang, M., Xiong, H., Fang, L., Zhang, X., Liu, C., and Wu, S. (2017). FK506 binding protein 10 is overexpressed and promotes renal cell carcinoma. Urol. Int. *98*, 169–176. https://doi.org/10.1159/000448338.
34. Yang, Y., Wang, J., Xu, S., Shi, F., and Shan, A. (2020). Calumenin contributes to epithelial-mesenchymal transition and predicts poor survival in glioma. Preprint at bioRxiv. https://doi.org/10.1101/2020.07.05.188318.
35. Han, M.Z., Xu, R., Xu, Y.Y., Zhang, X., Ni, S.L., Huang, B., Chen, A.J., Wei, Y.Z., Wang, S., Li, W.J., et al. (2017). TAGLN2 is a candidate prognostic biomarker promoting tumorigenesis in human gliomas. J. Exp. Clin. Cancer Res. *36*, 155. https://doi.org/10.1186/s13046-017-0619-9.
36. Tsai, C.-K., Huang, L.-C., Tsai, W.-C., Huang, S.-M., Lee, J.-T., and Hueng, D.-Y. (2018). Overexpression of PLOD3 promotes tumor progression and poor prognosis in gliomas. Oncotarget *9*, 15705–15720. https://doi.org/10.18632/oncotarget.24594.
37. Tantyo, N.A., Karyadi, A.S., Rasman, S.Z., Salim, M.R.G., Devina, A., and Sumarpo, A. (2019). The prognostic value of S100A10 expression in cancer. Oncol. Lett. *17*, 1417–1424. https://doi.org/10.3892/ol.2018.9751.
38. Nikas, J.B. (2016). Independent validation of a mathematical genomic model for survival of glioma patients. Am. J. Cancer Res. *6*, 1408–1419.
39. Sinha, S., Bheemsetty, V.A., and Inamdar, M.S. (2018). A double helical motif in OCIAD2 is essential for its localization, interactions and STAT3 activation. Sci. Rep. *8*, 7362. https://doi.org/10.1038/s41598-018-25667-3.
40. Gai, X., Tu, K., Lu, Z., and Zheng, X. (2014). MRC2 expression correlates with TGFβ1 and survival in hepatocellular carcinoma. Int. J. Mol. Sci. *15*, 15011–15025. https://doi.org/10.3390/ijms150915011.
41. Liu, D., Li, W., Zhong, F., Yin, J., Zhou, W., Li, S., Sun, X., Xu, J., Li, G., Wen, Y., et al. (2020). METTL7B is required for cancer cell proliferation and tumorigenesis in non-small cell lung cancer. Front. Pharmacol. *11*, 178. https://doi.org/10.3389/fphar.2020.00178.
42. Setti, M., Savalli, N., Osti, D., Richichi, C., Angelini, M., Brescia, P., Fornasari, L., Carro, M.S., Mazzanti, M., and Pelicci, G. (2013). Functional role of CLIC1 ion channel in glioblastoma-derived stem/progenitor cells. J. Natl. Cancer Inst. *105*, 1644–1655. https://doi.org/10.1093/jnci/djt278.
43. Wang, Z., Wang, X., Zhang, N., Zhang, H., Dai, Z., Zhang, M., Feng, S., and Cheng, Q. (2020). Pentraxin 3 promotes glioblastoma progression by negative regulating cells autophagy. Front. Cell Dev. Biol. *8*, 795. https://doi.org/10.3389/fcell.2020.00795.
44. Chou, A.P., Chowdhury, R., Li, S., Chen, W., Kim, A.J., Piccioni, D.E., Selfridge, J.M., Mody, R.R., Chang, S., Lalezari, S., et al. (2012). Identification of retinol binding protein 1 promoter hypermethylation in isocitrate dehydrogenase 1 and 2 mutant gliomas. J. Natl. Cancer Inst. *104*, 1458–1469. https://doi.org/10.1093/jnci/djs357.
45. Ju Lee, H., Bartsch, D., Xiao, C., Guerrero, S., Ahuja, G., Schindler, C., Moresco, J.J., Yates, J.R., Gebauer, F., Bazzi, H., et al. (2017). A post-transcriptional program coordinated by CSDE1 prevents intrinsic neural differentiation of human embryonic stem cells. Nat. Commun. *8*, 1456. https://doi.org/10.1038/s41467-017-01744-5.
46. Martinez-Useros, J., Garcia-Carbonero, N., Li, W., Fernandez-Aceñero, M.J., Cristobal, I., Rincon, R., Rodriguez-Remirez, M., Borrero-Palacios, A., and Garcia-Foncillas, J. (2019). UNR/CSDE1 expression is critical to maintain invasive phenotype of colorectal cancer through regulation of c-MYC and epithelial-to-mesenchymal transition. J. Clin. Med. *8*, 560. https://doi.org/10.3390/jcm8040560.
47. Eckert, M.A., Coscia, F., Chryplewicz, A., Chang, J.W., Hernandez, K.M., Pan, S., Tienda, S.M., Nahotko, D.A., Li, G., Blaženović, I., et al. (2019). Proteomics reveals NNMT as a master metabolic regulator of cancer-associated fibroblasts. Nature *569*, 723–728. https://doi.org/10.1038/s41586-019-1173-8.
48. Kapoor, A., Goldberg, M.S., Cumberland, L.K., Ratnakumar, K., Segura, M.F., Emanuel, P.O., Menendez, S., Vardabasso, C., LeRoy, G., Vidal, C.I., et al. (2010). The histone variant macroH2A suppresses melanoma progression through regulation of CDK8. Nature *468*, 1105–1109. https://doi.org/10.1038/nature09590.
49. Wang, Y., Zhao, W., Liu, X., Guan, G., and Zhuang, M. (2019). ARL3 is downregulated and acts as a prognostic biomarker in glioma. J. Transl. Med. *17*, 210–215. https://doi.org/10.1186/s12967-019-1914-3.

50. Wang, R., Gurguis, C.I., Gu, W., Ko, E.A., Lim, I., Bang, H., Zhou, T., and Ko, J.H. (2015). Ion channel gene expression predicts survival in glioma patients. Sci. Rep. *5*, 11593. https://doi.org/10.1038/srep11593.

51. Fu, H., Ge, B., Chen, D., Wu, Y., Luo, Q., Li, X., Zheng, C., and Tang, Q. (2019). Phytanoyl-CoA 2-hydroxylase-interacting protein-like gene is a therapeutic target gene for glioblastoma multiforme. Med. Sci. Monit. *25*, 2583–2590. https://doi.org/10.12659/MSM.913895.

52. Zhao, S.F., Wang, S.G., Zhao, Z.Y., and Li, W.L. (2019). AKR1C1-3, notably AKR1C3, are distinct biomarkers for liver cancer diagnosis and prognosis: database mining in malignancies. Oncol. Lett. *18*, 4515–4522. https://doi.org/10.3892/ol.2019.10802.

53. Wang, B., Gu, Y., Hui, K., Huang, J., Xu, S., Wu, S., Li, L., Fan, J., Wang, X., Hsieh, J.T., et al. (2018). AKR1C3, a crucial androgenic enzyme in prostate cancer, promotes epithelial-mesenchymal transition and metastasis through activating ERK signaling. Urol. Oncol. *36*, 472.e11–472.e20. https://doi.org/10.1016/j.urolonc.2018.07.005.

54. Cheung, H.C., Hai, T., Zhu, W., Baggerly, K.A., Tsavachidis, S., Krahe, R., and Cote, G.J. (2009). Splicing factors PTBP1 and PTBP2 promote proliferation and migration of glioma cell lines. Brain *132*, 2277–2288. https://doi.org/10.1093/brain/awp153.

55. Brellier, F., Ruggiero, S., Zwolanek, D., Martina, E., Hess, D., Brown-Luedi, M., Hartmann, U., Koch, M., Merlo, A., Lino, M., and Chiquet-Ehrismann, R. (2011). SMOC1 is a tenascin-C interacting protein over-expressed in brain tumors. Matrix Biol. *30*, 225–233. https://doi.org/10.1016/j.matbio.2011.02.001.

56. Johnson, G.S., Rajendran, P., and Dashwood, R.H. (2020). CCAR1 and CCAR2 as gene chameleons with antagonistic duality: preclinical, human translational, and mechanistic basis. Cancer Sci. *111*, 3416–3425. https://doi.org/10.1111/cas.14579.

57. Maurya, P.K., Mishra, A., Yadav, B.S., Singh, S., Kumar, P., Chaudhary, A., Srivastava, S., Murugesan, S.N., and Mani, A. (2017). Role of Y box protein-1 in cancer: as potential biomarker and novel therapeutic target. J. Cancer *8*, 1900–1907. https://doi.org/10.7150/jca.17689.

58. Kuwano, M., Shibata, T., Watari, K., and Ono, M. (2019). Oncogenic Y-box binding protein-1 as an effective therapeutic target in drug-resistant cancer. Cancer Sci. *110*, 1536–1543. https://doi.org/10.1111/cas.14006.

59. Gupta, M.K., Polisetty, R.V., Sharma, R., Ganesh, R.A., Gowda, H., Purohit, A.K., Ankathi, P., Prasad, K., Mariswamappa, K., Lakshmikantha, A., et al. (2019). Altered transcriptional regulatory proteins in glioblastoma and YBX1 as a potential regulator of tumor invasion. Sci. Rep. *9*, 10986. https://doi.org/10.1038/s41598-019-47360-9.

60. Jia, W., Chen, P., and Cheng, Y. (2019). PRDX4 and its roles in various cancers. Technol. Cancer Res. Treat. *18*, 1533033819864313. https://doi.org/10.1177/1533033819864313.

61. Kim, T.H., Song, J., Alcantara Llaguno, S.R., Murnan, E., Liyanarachchi, S., Palanichamy, K., Yi, J.Y., Viapiano, M.S., Nakano, I., Yoon, S.O., et al. (2012). Suppression of peroxiredoxin 4 in glioblastoma cells increases apoptosis and reduces tumor growth. PLoS One *7*, e42818. https://doi.org/10.1371/journal.pone.0042818.

62. Chen, R., Zhu, J., Dong, Y., He, C., and Hu, X. (2015). Suppressor of Ty homolog-5, a novel tumor-specific human telomerase reverse transcriptase promoter-binding protein and activator in colon cancer cells. Oncotarget *6*, 32841–32855. https://doi.org/10.18632/oncotarget.5301.

63. Govaere, O., Petz, M., Wouters, J., Vandewynckel, Y.P., Scott, E.J., Topal, B., Nevens, F., Verslype, C., Anstee, Q.M., Van Vlierberghe, H., et al. (2017). The PDGFRα-laminin B1-keratin 19 cascade drives tumor progression at the invasive front of human hepatocellular carcinoma. Oncogene *36*, 6605–6616. https://doi.org/10.1038/onc.2017.260.

64. Hsiao, K.C., Chu, P.Y., Chang, G.C., and Liu, K.J. (2020). Elevated expression of lumican in lung cancer cells promotes bone metastasis through an autocrine regulatory mechanism. Cancers *12*, 233. https://doi.org/10.3390/cancers12010233.

65. Graille, M., and Rougemaille, M. (2020). ERH proteins: connecting RNA processing to tumorigenesis? Curr. Genet. *66*, 689–692. https://doi.org/10.1007/s00294-020-01065-z.

66. Pang, K., Zhang, Z., Hao, L., Shi, Z., Chen, B., Zang, G., Dong, Y., Li, R., Liu, Y., Wang, J., et al. (2019). The ERH gene regulates migration and invasion in 5637 and T24 bladder cancer cells. BMC Cancer *19*, 225. https://doi.org/10.1186/s12885-019-5423-9.

67. Zhang, D., Chu, Y.J., Song, K.J., Chen, Y.L., Liu, W., Lv, T., Wang, J., Zhao, H., Ren, Y.Z., Xu, J.X., et al. (2020). Knockdown of enhancer of rudimentary homolog inhibits proliferation and metastasis in ovarian cancer by regulating epithelial-mesenchymal transition. Biomed. Pharmacother. *125*, 109974. https://doi.org/10.1016/j.biopha.2020.109974.

68. Gawrzak, S., Rinaldi, L., Gregorio, S., Arenas, E.J., Salvador, F., Urosevic, J., Figueras-Puig, C., Rojo, F., Del Barco Barrantes, I., Cejalvo, J.M., et al. (2018). MSK1 regulates luminal cell differentiation and metastatic dormancy in ER + breast cancer. Nat. Cell Biol. *20*, 211–221. https://doi.org/10.1038/s41556-017-0021-z.

69. Wu, S., Wang, S., Zheng, S., Verhaak, R., Koul, D., and Yung, W.K.A. (2016). MSK1-Mediated βb-catenin phosphorylation confers resistance to PI3K/mTOR inhibitors in glioblastoma. Mol. Cancer Ther. *15*, 1656–1668. https://doi.org/10.1158/1535-7163.MCT-15-0857.

70. Zhou, X., Xia, E., Bhandari, A., Zheng, C., Xiang, J., Guan, Y., and Zhang, X. (2018). LRP4 promotes proliferation, migration, and invasion in papillary thyroid cancer. Biochem. Biophys. Res. Commun. *503*, 257–263. https://doi.org/10.1016/j.bbrc.2018.06.012.

71. Jiang, J., Ren, H., Xu, Y., Wudu, M., Wang, Q., Liu, Z., Su, H., Jiang, X., Zhang, Y., Zhang, B., and Qiu, X. (2020). TRIM67 promotes the proliferation, migration, and invasion of non-small-cell lung cancer by positively regulating the Notch pathway. J. Cancer *11*, 1240–1249. https://doi.org/10.7150/jca.38286.

72. Wang, S., Zhang, Y., Huang, J., Wong, C.C., Zhai, J., Li, C., Wei, G., Zhao, L., Wang, G., Wei, H., et al. (2019). TRIM67 activates p53 to suppress colorectal cancer initiation and progression. Cancer Res. *79*, 4086–4098. https://doi.org/10.1158/0008-5472.CAN-18-3614.

73. Kanda, M., Nomoto, S., Okamura, Y., Hayashi, M., Hishida, M., Fujii, T., Nishikawa, Y., Sugimoto, H., Takeda, S., and Nakao, A. (2011). Promoter hypermethylation of fibulin 1 gene is associated with tumor progression in hepatocellular carcinoma. Mol. Carcinog. *50*, 571–579. https://doi.org/10.1002/mc.20735.

74. Xiao, W., Wang, J., Li, H., Xia, D., Yu, G., Yao, W., Yang, Y., Xiao, H., Lang, B., Ma, X., et al. (2014). Fibulin-1 is epigenetically down-regulated and related with bladder cancer recurrence. BMC Cancer *14*, 677. https://doi.org/10.1186/1471-2407-14-677.

75. Xia, S., Lal, B., Tung, B., Wang, S., Goodwin, C.R., and Laterra, J. (2016). Tumor microenvironment tenascin-C promotes glioblastoma invasion and negatively regulates tumor proliferation. Neuro Oncol. *18*, 507–517. https://doi.org/10.1093/neuonc/nov171.

76. Yoshida, T., Akatsuka, T., and Imanaka-Yoshida, K. (2015). Tenascin-C and integrins in cancer. Cell Adh. Migr. *9*, 96–104. https://doi.org/10.1080/19336918.2015.1008332.

77. Ye, Y.P., Jiao, H.L., Wang, S.Y., Xiao, Z.Y., Zhang, D., Qiu, J.F., Zhang, L.J., Zhao, Y.L., Li, T.T., Li-Liang, et al. (2018). Hypermethylation of DMTN promotes the metastasis of colorectal cancer cells by regulating the actin cytoskeleton through Rac1 signaling activation 11 Medical and Health Sciences 1112 Oncology and Carcinogenesis 06 Biological Sciences 0604 Genetics. J. Exp. Clin. Cancer Res. *37*, 299. https://doi.org/10.1186/s13046-018-0958-1.

78. Sun, S.C. (2010). CYLD: a tumor suppressor deubiquitinase regulating NF-B activation and diverse biological processes. Cell Death Differ. *17*, 25–34. https://doi.org/10.1038/cdd.2009.43.

79. Zhang, X., Wang, J., Jia, Y., Liu, T., Wang, M., Lv, W., Zhang, R., Shi, J., and Liu, L. (2019). CDK5 neutralizes the tumor suppressing effect of BIN1 via mediating phosphorylation of c-MYC at Ser-62 site in NSCLC. Cancer Cell Int. *19*, 226. https://doi.org/10.1186/s12935-019-0952-5.

80. Nakahata, S., Ichikawa, T., Maneesaay, P., Saito, Y., Nagai, K., Tamura, T., Manachai, N., Yamakawa, N., Hamasaki, M., Kitabayashi, I., et al. (2014). Loss of NDRG2 expression activates PI3K-AKT signalling via PTEN phosphorylation in ATLL and other cancers. Nat. Commun. *5*, 3393. https://doi.org/10.1038/ncomms4393.

81. Bencivenga, D., Caldarelli, I., Stampone, E., Mancini, F.P., Balestrieri, M.L., Della Ragione, F., and Borriello, A. (2017). p27Kip1 and human cancers: a reappraisal of a still enigmatic protein. Cancer Lett. *403*, 354–365. https://doi.org/10.1016/j.canlet.2017.06.031.

82. Lobbous, M., Bernstock, J.D., Coffee, E., Friedman, G.K., Metrock, L.K., Chagoya, G., Elsayed, G., Nakano, I., Hackney, J.R., Korf, B.R., and Nabors, L.B. (2020). An update on neurofibromatosis type 1-associated gliomas. Cancers *12*, 114. https://doi.org/10.3390/cancers12010114.

83. Dashzeveg, N., and Yoshida, K. (2016). Crosstalk between tumor suppressors p53 and PKCδ: execution of the intrinsic apoptotic pathways. Cancer Lett. *377*, 158–163. https://doi.org/10.1016/j.canlet.2016.04.032.

84. Baumann, U., Fern'ndez-S'iz, V., Rudelius, M., Lemeer, S., Rad, R., Knorn, A.M., Slawska, J., Engel, K., Jeremias, I., Li, Z., et al. (2014). Disruption of the PRKCD-FBXO25-HAX-1 axis attenuates the apoptotic response and drives lymphomagenesis. Nat. Med. *20*, 1401–1409. https://doi.org/10.1038/nm.3740.

85. Allen-Petersen, B.L., Carter, C.J., Ohm, A.M., and Reyland, M.E. (2014). Protein kinase Cδ is required for ErbB2-driven mammary gland tumorigenesis and negatively correlates with prognosis in human breast cancer. Oncogene *33*, 1306–1315. https://doi.org/10.1038/onc.2013.59.

86. Bignone, P.A., Lee, K.Y., Liu, Y., Emilion, G., Finch, J., Soosay, A.E.R., Charnock, F.M.L., Beck, S., Dunham, I., Mungall, A.J., and Ganesan, T.S. (2007). RPS6KA2, a putative tumour suppressor gene at 6q27 in sporadic epithelial ovarian cancer. Oncogene *26*, 683–700. https://doi.org/10.1038/sj.onc.1209827.

87. Stone, A.R., Bobo, W., Brat, D.J., Devi, N.S., Van Meir, E.G., and Vertino, P.M. (2004). Aberrant methylation and down-regulation of TMS1/ASC in human glioblastoma. Am. J. Pathol. *165*, 1151–1161. https://doi.org/10.1016/S0002-9440(10)63376-7.

88. Sharma, N., Saxena, S., Agrawal, I., Singh, S., Srinivasan, V., Arvind, S., Epari, S., Paul, S., and Jha, S. (2019). Differential expression profile of NLRs and AIM2 in glioma and implications for NLRP12 in glioblastoma. Sci. Rep. *9*, 8480. https://doi.org/10.1038/s41598-019-44854-4.

89. Martinon, F., Burns, K., and Tschopp, J. (2002). The Inflammasome: a molecular platform triggering activation of inflammatory caspases and processing of proIL-β. Mol. Cell *10*, 417–426. https://doi.org/10.1016/S1097-2765(02)00599-3.

90. Behnan, J., Stangeland, B., Hosainey, S.A.M., Joel, M., Olsen, T.K., Micci, F., Glover, J.C., Isakson, P., and Brinchmann, J.E. (2017). Differential propagation of stroma and cancer stem cells dictates tumorigenesis and multipotency. Oncogene *36*, 570–584. https://doi.org/10.1038/onc.2016.230.

91. Figliuolo da Paz, V., Ghishan, F.K., and Kiela, P.R. (2020). Emerging roles of disabled homolog 2 (DAB2) in immune regulation. Front. Immunol. *11*, 580302–580311. https://doi.org/10.3389/fimmu.2020.580302.

92. Yamini, B. (2018). NF-κB, mesenchymal differentiation and glioblastoma. Cells *7*, 125. https://doi.org/10.3390/cells7090125.

93. Oprita, A., Baloi, S.C., Staicu, G.A., Alexandru, O., Tache, D.E., Danoiu, S., Micu, E.S., and Sevastre, A.S. (2021). Updated insights on EGFR signaling pathways in glioma. Int. J. Mol. Sci. *22*, 587. https://doi.org/10.3390/ijms22020587.

94. Pu, P., Kang, C., Li, J., Jiang, H., and Cheng, J. (2006). The effects of antisense AKT2 RNA on the Inhibition of malignant glioma cell growth in vitro and in vivo. J. Neuro Oncol. *76*, 1–11. https://doi.org/10.1007/s11060-005-3029-3.

95. Kim, E.H., Jo, Y., Sai, S., Park, M.J., Kim, J.Y., Kim, J.S., Lee, Y.J., Cho, J.M., Kwak, S.Y., Baek, J.H., et al. (2019). Tumor-treating fields induce autophagy by blocking the Akt2/miR29b axis in glioblastoma cells. Oncogene *38*, 6630–6646. https://doi.org/10.1038/s41388-019-0882-7.

96. Saito, S., Cigdem, S., Okuwaki, M., and Nagata, K. (2016). Leukemia-associated Nup214 fusion proteins disturb the XPO1-mediated nuclear-cytoplasmic transport pathway and thereby the NF-κB signaling pathway. Mol. Cell Biol. *36*, 1820–1835. https://doi.org/10.1128/mcb.00158-16.

97. Tao, T., Shi, Y., Han, D., Luan, W., Qian, J., Zhang, J., Wang, Y., and You, Y.; Chinese Glioma Cooperative Group CGCG (2014). TPM3, a strong prognosis predictor, is involved in malignant progression through MMP family members and EMT-like activators in gliomas. Tumour Biol. *35*, 9053–9059. https://doi.org/10.1007/s13277-014-1974-1.

98. Su, Y., Huang, J., and Hu, J. (2019). M6 a rna methylation regulators contribute to malignant progression and have clinical prognostic impact in gastric cancer. Front. Oncol. *9*, 1038. https://doi.org/10.3389/fonc.2019.01038.

99. Lee, Y., Lee, J.K., Ahn, S.H., Lee, J., and Nam, D.H. (2016). WNT signaling in glioblastoma and therapeutic opportunities. Lab. Invest. *96*, 137–150. https://doi.org/10.1038/labinvest.2015.140.

100. Zuccarini, M., Giuliani, P., Ziberi, S., Carluccio, M., Iorio, P.D., Caciagli, F., and Ciccarelli, R. (2018). The role of wnt signal in glioblastoma development and progression: a possible new pharmacological target for the therapy of this tumor. Genes *9*, 105. https://doi.org/10.3390/genes9020105.

101. Manoranjan, B., Chokshi, C., Venugopal, C., Subapanditha, M., Savage, N., Tatari, N., Provias, J.P., Murty, N.K., Moffat, J., Doble, B.W., and Singh, S.K. (2020). A CD133-AKT-Wnt signaling axis drives glioblastoma brain tumor-initiating cells. Oncogene *39*, 1590–1599. https://doi.org/10.1038/s41388-019-1086-x.

102. Chen, Y., Huang, Q., Liu, W., Zhu, Q., Cui, C.P., Xu, L., Guo, X., Wang, P., Liu, J., Dong, G., et al. (2018). Mutually exclusive acetylation and ubiquitylation of the splicing factor SRSF5 control tumor growth. Nat. Commun. *9*, 2464. https://doi.org/10.1038/s41467-018-04815-3.

103. Nandakumar, P., Mansouri, A., and Das, S. (2017). The role of ATRX in glioma biology. Front. Oncol. *7*, 236. https://doi.org/10.3389/fonc.2017.00236.

104. Clynes, D., Jelinska, C., Xella, B., Ayyub, H., Scott, C., Mitson, M., Taylor, S., Higgs, D.R., and Gibbons, R.J. (2015). Suppression of the alternative lengthening of telomere pathway by the chromatin remodelling factor ATRX. Nat. Commun. *6*, 7538. https://doi.org/10.1038/ncomms8538.

105. Mukherjee, J., Johannessen, T.C., Ohba, S., Chow, T.T., Jones, L., Pandita, A., and Pieper, R.O. (2018). Mutant IDH1 cooperates with ATRX loss to drive the alternative lengthening of telomere phenotype in glioma. Cancer Res. *78*, 2966–2977. https://doi.org/10.1158/0008-5472.CAN-17-2269.

106. Walsh, K.M., Wiencke, J.K., Lachance, D.H., Wiemels, J.L., Molinaro, A.M., Eckel-Passow, J.E., Jenkins, R.B., and Wrensch, M.R. (2015). Telomere maintenance and the etiology of adult glioma. Neuro Oncol. *17*, 1445–1452. https://doi.org/10.1093/neuonc/nov082.

107. Ferreira, M.S.V., Sørensen, M.D., Pusch, S., Beier, D., Bouillon, A.-S., Kristensen, B.W., Brümmendorf, T.H., Beier, C.P., and Beier, F. (2020). Alternative lengthening of telomeres is the major telomere maintenance mechanism in astrocytoma with isocitrate dehydrogenase 1 mutation. J. Neuro Oncol. *147*, 1–14. https://doi.org/10.1007/s11060-020-03394-y.

108. Körber, V., Yang, J., Barah, P., Wu, Y., Stichel, D., Gu, Z., Fletcher, M.N.C., Jones, D., Hentschel, B., Lamszus, K., et al. (2019). Evolutionary trajectories of IDH WT glioblastomas reveal a common path of early tumorigenesis instigated years ahead of initial diagnosis. Cancer Cell *35*, 692–704.e12. https://doi.org/10.1016/j.ccell.2019.02.007.

109. Crespo, I., Vital, A.L., Nieto, A.B., Rebelo, O., Tão, H., Lopes, M.C., Oliveira, C.R., French, P.J., Orfao, A., and Tabernero, M.D. (2011). Detailed characterization of alterations of chromosomes 7, 9, and 10 in

glioblastomas as assessed by single-nucleotide polymorphism arrays. J. Mol. Diagn. *13*, 634–647. https://doi.org/10.1016/j.jmoldx.2011.06.003.

110. Lopez-Gines, C., Cerda-Nicolas, M., Gil-Benso, R., Pellin, A., Lopez-Guerrero, J.A., Callaghan, R., Benito, R., Roldan, P., Piquer, J., Llacer, J., and Barbera, J. (2005). Association of chromosome 7, chromosome 10 and EGFR gene amplification in glioblastoma multiforme. Clin. Neuropathol. *24*, 209–218.

111. Leone, G., Abla, H., Gasparre, G., Porcelli, A.M., and Iommarini, L. (2018). The oncojanus paradigm of respiratory complex I. Genes *9*, 243. https://doi.org/10.3390/genes9050243.

112. Sen, T., Sen, N., Noordhuis, M.G., Ravi, R., Wu, T.C., Ha, P.K., Sidransky, D., and Hoque, M.O. (2012). OGDHL is a modifier of AKT-dependent signaling and NF-κB function. PLoS One *7*, e48770. https://doi.org/10.1371/journal.pone.0048770.

113. Tseng, P.L., Chen, C.W., Hu, K.H., Cheng, H.C., Lin, Y.H., Tsai, W.H., Cheng, T.J., Wu, W.H., Yeh, C.W., Lin, C.C., et al. (2018). The decrease of glycolytic enzyme hexokinase 1 accelerates tumor malignancy via deregulating energy metabolism but sensitizes cancer cells to 2-deoxyglucose inhibition. Oncotarget *9*, 18949–18969. https://doi.org/10.18632/oncotarget.24855.

114. Formentini, L., S'nchez-Aragó, M., S'nchez-Cenizo, L., and Cuezva, J.M. (2012). The mitochondrial ATPase inhibitory factor 1 triggers a ROS-mediated retrograde prosurvival and proliferative response. Mol. Cell *45*, 731–742. https://doi.org/10.1016/j.molcel.2012.01.008.

115. García-Bermúdez, J., S'nchez-Aragó, M., Soldevilla, B., Del Arco, A., Nuevo-Tapioles, C., and Cuezva, J.M. (2015). PKA phosphorylates the ATPase inhibitory factor 1 and inactivates its capacity to bind and inhibit the mitochondrial H(+)-ATP synthase. Cell Rep. *12*, 2143–2155. https://doi.org/10.1016/j.celrep.2015.08.052.

116. Lymbouridou, R., Soufla, G., Chatzinikola, A.M., Vakis, A., and Spandidos, D.A. (2009). Down-regulation of K-ras and H-ras in human brain gliomas. Eur. J. Cancer *45*, 1294–1303. https://doi.org/10.1016/j.ejca.2008.12.028.

117. Timofeev, O., Cizmecioglu, O., Settele, F., Kempf, T., and Hoffmann, I. (2010). Cdc25 phosphatases are required for timely assembly of CDK1-cyclin B at the G2/M transition. J. Biol. Chem. *285*, 16978–16990. https://doi.org/10.1074/jbc.M109.096552.

118. Zhou, Y., Shen, J.K., Hornicek, F.J., Kan, Q., and Duan, Z. (2016). The emerging roles and therapeutic potential of cyclin-dependent kinase 11 (CDK11) in human cancer. Oncotarget *7*, 40846–40859. https://doi.org/10.18632/oncotarget.8519.

119. Wong, D., Lee, T.H., Lum, A., Tao, V.L., and Yip, S. (2022). Integrated proteomic analysis of low-grade gliomas reveals contributions of 1p-19q co-deletion to oligodendroglioma. Acta Neuropathol. Commun. *10*, 70. https://doi.org/10.1186/s40478-022-01372-1.

120. Oh, S., Yeom, J., Cho, H.J., Kim, J.-H., Yoon, S.-J., Kim, H., Sa, J.K., Ju, S., Lee, H., Oh, M.J., et al. (2020). Integrated pharmaco-proteogenomics defines two subgroups in isocitrate dehydrogenase wild-type glioblastoma with prognostic and therapeutic opportunities. Nat. Commun. *11*, 3288. https://doi.org/10.1038/s41467-020-17139-y.

121. Stupp, R., Mason, W.P., van den Bent, M.J., Weller, M., Fisher, B., Taphoorn, M.J.B., Belanger, K., Brandes, A.A., Marosi, C., Bogdahn, U., et al. (2005). Radiotherapy plus concomitant and adjuvant temozolomide for glioblastoma. N. Engl. J. Med. *352*, 987–996. https://doi.org/10.1056/NEJMoa043330.

122. van den Bent, M.J., Tesileanu, C.M.S., Wick, W., Sanson, M., Brandes, A.A., Clement, P.M., Erridge, S., Vogelbaum, M.A., Nowak, A.K., Baurain, J.F., et al. (2021). Adjuvant and concurrent temozolomide for 1p/19q non-co-deleted anaplastic glioma (CATNON; EORTC study 26053-22054): second interim analysis of a randomised, open-label, phase 3 study. Lancet Oncol. *22*, 813–823. https://doi.org/10.1016/S1470-2045(21)00090-5.

123. Garofano, L., Migliozzi, S., Oh, Y.T., D'Angelo, F., Najac, R.D., Ko, A., Frangaj, B., Caruso, F.P., Yu, K., Yuan, J., et al. (2021). Pathway-based classification of glioblastoma uncovers a mitochondrial subtype with therapeutic vulnerabilities. Nat. Cancer *2*, 141–156. https://doi.org/10.1038/s43018-020-00159-4.

124. Mund, A., Coscia, F., Hollandi, R., Kov'cs, F., Kriston, A., Brunner, A.-D., Bzorek, M., Naimy, S., Rahbek Gjerdrum, L.M., Dyring-Andersen, B., et al. (2021). AI-driven Deep Visual Proteomics defines cell identity and heterogeneity. Preprint at bioRxiv. https://doi.org/10.1101/2021.01.25.427969.

125. Richardson, R.B., and Harper, M.-E. (2016). Mitochondrial stress controls the radiosensitivity of the oxygen effect: implications for radiotherapy. Oncotarget *7*, 21469–21483. https://doi.org/10.18632/oncotarget.7412.

126. Mellinghoff, I.K., Ellingson, B.M., Touat, M., Maher, E., De La Fuente, M.I., Holdhoff, M., Cote, G.M., Burris, H., Janku, F., Young, R.J., et al. (2020). Ivosidenib in isocitrate dehydrogenase 1-mutated advanced glioma. J. Clin. Oncol. *38*, 3398–3406. https://doi.org/10.1200/JCO.19.03327.

127. Zarei, M., Hue, J.J., Hajihassani, O., Graor, H.J., Katayama, E.S., Loftus, A.W., Bajor, D., Rothermel, L.D., Vaziri-Gohar, A., and Winter, J.M. (2022). Clinical development of IDH1 inhibitors for cancer therapy. Cancer Treat Rev. *103*, 102334. https://doi.org/10.1016/j.ctrv.2021.102334.

128. Mazurek, M., Litak, J., Kamieniak, P., Kulesza, B., Jonak, K., Baj, J., and Grochowski, C. (2020). Metformin as potential therapy for high-grade glioma. Cancers *12*, 210. https://doi.org/10.3390/cancers12010210.

129. Valtorta, S., Lo Dico, A., Raccagni, I., Gaglio, D., Belloli, S., Politi, L.S., Martelli, C., Diceglie, C., Bonanomi, M., Ercoli, G., et al. (2017). Metformin and temozolomide, a synergic option to overcome resistance in glioblastoma multiforme models. Oncotarget *8*, 113090–113104. https://doi.org/10.18632/oncotarget.23028.

130. Sharma, K., Schmitt, S., Bergner, C.G., Tyanova, S., Kannaiyan, N., Manrique-Hoyos, N., Kongi, K., Cantuti, L., Hanisch, U.-K., Philips, M.-A., et al. (2015). Cell type- and brain region-resolved mouse brain proteome. Nat. Neurosci. *18*, 1819–1831.

131. Cox, J., and Mann, M. (2008). MaxQuant enables high peptide identification rates, individualized p.p.b.-range mass accuracies and proteome-wide protein quantification. Nat. Biotechnol. *26*, 1367–1372. https://doi.org/10.1038/nbt.1511.

132. Tyanova, S., Temu, T., Sinitcyn, P., Carlson, A., Hein, M.Y., Geiger, T., Mann, M., and Cox, J. (2016). The Perseus computational platform for comprehensive analysis of (prote)omics data. Nat. Methods *13*, 731–740. https://doi.org/10.1038/nmeth.3901.

133. Suwala, A.K., Felix, M., Friedel, D., Stichel, D., Schrimpf, D., Hinz, F., Hewer, E., Schweizer, L., Dohmen, H., Pohl, U., et al. (2022). Oligosarcomas, IDH-mutant are distinct and aggressive. Acta Neuropathol. *143*, 263–281. https://doi.org/10.1007/s00401-021-02395-z.

134. V Hovestadt, M Zapatka. conumee: enhanced copy-number variation analysis using Illumina DNA methylation arrays.

135. Gu, Z., Eils, R., and Schlesner, M. (2016). Complex heatmaps reveal patterns and correlations in multidimensional genomic data. Bioinformatics *32*, 2847–2849. https://doi.org/10.1093/bioinformatics/btw313.

136. Therneau, T M; Lumley, T; Atkinson, E; Crowson, C. Survival (R Package).

137. Kassambra, A; Kosinski, M; Biecek, P; Scheipl, F. Survminer (R Package).

138. Radke, J., Koch, A., Pritsch, F., Schumann, E., Misch, M., Hempt, C., Lenz, K., Löbel, F., Paschereit, F., Heppner, F.L., et al. (2019). Predictive MGMT status in a homogeneous cohort of IDH wildtype glioblastoma patients. Acta Neuropathol. Commun. *7*, 89. https://doi.org/10.1186/s40478-019-0745-z.

139. Lohkamp, L.N., Schinz, M., Gehlhaar, C., Guse, K., Thomale, U.W., Vajkoczy, P., Heppner, F.L., and Koch, A. (2016). MGMT Promoter methylation and BRAF V600E mutations are helpful markers to discriminate

pleomorphic xanthoastrocytoma from giant cell glioblastoma. PLoS One *11*, e0156422. https://doi.org/10.1371/journal.pone.0156422.

140. Kulak, N.A., Pichler, G., Paron, I., Nagaraj, N., and Mann, M. (2014). Minimal, encapsulated proteomic-sample processing applied to copy-number estimation in eukaryotic cells. Nat. Methods *11*, 319–324. https://doi.org/10.1038/nmeth.2834.

141. Robinson, J.T., Thorvaldsdóttir, H., Winckler, W., Guttman, M., Lander, E.S., Getz, G., and Mesirov, J.P. (2011). Integrative genomics viewer. Nat. Biotechnol. *29*, 24–26. https://doi.org/10.1038/nbt.1754.

142. Tusher, V.G., Tibshirani, R., and Chu, G. (2001). Significance analysis of microarrays applied to the ionizing radiation response. Proc. Natl. Acad. Sci. USA *98*, 5116–5121. https://doi.org/10.1073/pnas.091062498.

143. Wiestler, B., Capper, D., Holland-Letz, T., Korshunov, A., Von Deimling, A., Pfister, S.M., Platten, M., Weller, M., and Wick, W. (2013). ATRX loss refines the classification of anaplastic gliomas and identifies a subgroup of IDH mutant astrocytic tumors with better prognosis. Acta Neuropathol. *126*, 443–451. https://doi.org/10.1007/s00401-013-1156-z.

144. Cox, J., and Mann, M. (2012). 1D and 2D annotation enrichment: a statistical method integrating quantitative proteomics with complementary high-throughput data. BMC Bioinformatics *13*, S12. https://doi.org/10.1186/1471-2105-13-S16-S12.

145. Alečković, M., Wei, Y., LeRoy, G., Sidoli, S., Liu, D.D., Garcia, B.A., and Kang, Y. (2017). Identification of Nidogen 1 as a lung metastasis protein through secretome analysis. Genes Dev. *31*, 1439–1455. https://doi.org/10.1101/gad.301937.117.

146. Han, C., Liao, X., Qin, W., Yu, L., Liu, X., Chen, G., Liu, Z., Lu, S., Chen, Z., Su, H., et al. (2016). EGFR and SYNE2 are associated with p21 expression and SYNE2 variants predict post-operative clinical outcomes in HBV-related hepatocellular carcinoma. Sci. Rep. *6*, 31237. https://doi.org/10.1038/srep31237.

147. Gordon-Weeks, A., Lim, S.Y., Yuzhalin, A., and Lucotti, S. (2019). Tumour-derived laminin α5 (LAMA5) promotes colorectal liver metastasis growth, branching angiogenesis and notch pathway inhibition. Cancers *11*.

148. Fozzatti, L., Park, J.W., Zhao, L., Willingham, M.C., and Cheng, S.Y. (2013). Oncogenic actions of the nuclear receptor corepressor (NCOR1) in a mouse model of thyroid cancer. PLoS One *8*, e67954. https://doi.org/10.1371/journal.pone.0067954.

149. Zhao, J., Sun, Y., Huang, Y., Song, F., Huang, Z., Bao, Y., Zuo, J., Saffen, D., Shao, Z., Liu, W., and Wang, Y. (2017). Functional analysis reveals that RBM10 mutations contribute to lung adenocarcinoma pathogenesis by deregulating splicing. Sci. Rep. *7*, 40488. https://doi.org/10.1038/srep40488.

150. Feng, T., Liu, Y., Li, C., Li, Z., and Cai, H. (2017). DEK proto-oncogene is highly expressed in astrocytic tumors and regulates glioblastoma cell proliferation and apoptosis. Tumour Biol. *39*, 1010428317716248. https://doi.org/10.1177/1010428317716248.

151. Baskin, R., Woods, N.T., Mendoza-Fandiño, G., Forsyth, P., Egan, K.M., and Monteiro, A.N.A. (2015). Functional analysis of the 11q23.3 glioma susceptibility locus implicates PHLDB1 and DDX6 in glioma susceptibility. Sci. Rep. *5*, 17367. https://doi.org/10.1038/srep17367.

152. Taniguchi, K., Iwatsuki, A., Sugito, N., Shinohara, H., Kuranaga, Y., Oshikawa, Y., Tajirika, T., Futamura, M., Yoshida, K., Uchiyama, K., and Akao, Y. (2018). Oncogene RNA helicase DDX6 promotes the process of c-Myc expression in gastric cancer cells. Mol. Carcinog. *57*, 579–589. https://doi.org/10.1002/mc.22781.

153. Arentz, G., Chataway, T., Price, T.J., Izwan, Z., Hardi, G., Cummins, A.G., and Hardingham, J.E. (2011). Desmin expression in colorectal cancer stroma correlates with advanced stage disease and marks angiogenic microvessels. Clin. Proteomics *8*, 16. https://doi.org/10.1186/1559-0275-8-16.

154. Wang, Z., Kang, J., Deng, X., Guo, B., Wu, B., and Fan, Y. (2017). Knockdown of GATAD2A suppresses cell proliferation in thyroid cancer in vitro. Oncol. Rep. *37*, 2147–2152. https://doi.org/10.3892/or.2017.5436.

155. Anchi, T., Tamura, K., Furihata, M., Satake, H., Sakoda, H., Kawada, C., Kamei, M., Shimamoto, T., Fukuhara, H., Fukata, S., et al. (2012). SNRPE is involved in cell proliferation and progression of high-grade prostate cancer through the regulation of androgen receptor expression. Oncol. Lett. *3*, 264–268. https://doi.org/10.3892/ol.2011.505.

156. Wculek, S.K., and Malanchi, I. (2015). Neutrophils support lung colonization of metastasis-initiating breast cancer cells. Nature *528*, 413–417. https://doi.org/10.1038/nature16140.

157. Ivanova, A.V., Goparaju, C.M.V., Ivanov, S.V., Nonaka, D., Cruz, C., Beck, A., Lonardo, F., Wali, A., and Pass, H.I. (2009). Protumorigenic role of HAPLN1 and its IgV domain in malignant pleural mesothelioma. Clin. Cancer Res. *15*, 2602–2611. https://doi.org/10.1158/1078-0432.CCR-08-2755.

158. Yang, J., Yu, D., Liu, X., Changyong, E., and Yu, S. (2020). LINC00641/miR-4262/NRGN axis confines cell proliferation in glioma. Cancer Biol. Ther. *21*, 758–766. https://doi.org/10.1080/15384047.2020.1776581.

159. Beltran, A.S., Russo, A., Lara, H., Fan, C., Lizardi, P.M., and Blancafort, P. (2011). Suppression of breast tumor growth and metastasis by an engineered transcription factor. PLoS One *6*, e24595. https://doi.org/10.1371/journal.pone.0024595.

160. Zhou, C., Yu, J., Wang, M., Yang, J., Xiong, H., Huang, H., Wu, D., Hu, S., Wang, Y., Chen, X.Z., and Tang, J. (2017). Identification of glycerol-3-phosphate dehydrogenase 1 as a tumour suppressor in human breast cancer. Oncotarget *8*, 101309–101324. https://doi.org/10.18632/oncotarget.21087.

STAR★METHODS

KEY RESOURCES TABLE

REAGENT or RESOURCE	SOURCE	IDENTIFIER
Biological samples		
FFPE glioma tissue samples	Department of Neuropathology Charité - Universitätsmedizin Berlin	See Data S1 for each sample
Chemicals, peptides, and recombinant proteins		
lysyl Endopeptidase®, Mass Spectrometry Grade (Lys-C)	FUJIFILM Wako	WAKO 129-02541
trypsin, porcine, Mass Spectrometry Grade	Sigma Aldrich/Merck	Cat# T6567
styroldivinylbenzol-reversed phase sulfonate (SDB-RPS)	Empore 3M	Cat# 13427427
IDH1 R132H antibody	DIANOVA, clone H09	Cat# DIA-H09-L
Polymerase for IDH1 and IDH2 pyrosequencing	HotStarTag DNA Polymerase, Qiagen	Cat# 203205
Critical commercial assays		
Pierce BCA assay	Thermo Fisher	Cat# 23227
AssayMAP Cartridge Rack Fe(III)-NTA 5μL	Agilent Technologies	Cat# G5496-60085
Qiagen DNeasy blood and tissue DNA extraction kit	Qiagen	Cat# 69581
Maxwell RSC FFPE Plus DNA Purification Kit	Promega	Cat# AS1720
Zymo EZ Methylation Kit	Zymo Research Irvine	Cat# D5004
Infinium HD FFPE DNA Restore Kit	Illumina	Cat# WG-321-1002
Deposited data		
Mass spectrometric raw data	This study	PRIDE repositorium: PXD024427
Methylation and copy number variation raw data	This study	https://www.ncbi.nlm.nih.gov/geo/query/acc.cgi?acc=GSE212838
Murine brain proteome dataset	Sharma et al., 2015[130]	Table S5
CPTAC/Wang et al. glioma proteome dataset: sample annotations	Wang et al., 2021[25]	Table S1
CPTAC/Wang et al. glioma proteome dataset: protein intensities	Wang et al., 2021[25]	Table S2, Table 8 "proteome_normalized"
Oh et al. glioma proteome dataset: sample annotations	Oh et al., 2020[120]	Data S1
Oh et al. glioma proteome dataset: sample annotations	Oh et al., 2020[120]	Data S2, Table 2 "Global"
Wong et al. glioma proteome dataset: sample annotations	Wong et al., 2022[119]	https://github.com/derekwong90/LGG_proteomics/blob/main/data/metadata.txt
Wong et al. glioma proteome dataset: protein intensities	Wong et al., 2022[119]	https://github.com/derekwong90/LGG_proteomics/blob/main/data/protein_abundance.txt
Software and algorithms		
Xcalibur	Thermo Fisher Scientific	OPTON-30965
MaxQuant	Cox and Mann, 2008[131]	https://maxquant.org/
Perseus	Tyanova et al., 2016[132]	https://maxquant.org/perseus/
R	The R Project for Statistical Computing	https://www.r-project.org/

(*Continued on next page*)

Continued

REAGENT or RESOURCE	SOURCE	IDENTIFIER
Brain tumor classifier version v11b4	Capper et al., 2018[14]	www.molecularNeuropathology.org; Classifier Version v11b4
Brain tumor classifier version v12.5	Suwala et al., 2022[133]	www.molecularNeuropathology.org; Classifier Version v12.5
R/Bioconductor conumee package version 1.9.0	Hovestadt and Zapatka[134]	https://bioconductor.org/packages/release/bioc/html/conumee.html
R package ComplexHeatmaps v2.10.0	Gu et al., 2016[135]	https://www.bioconductor.org/packages/release/bioc/html/ComplexHeatmap.html
R package survival v3.1-8	Therneau et al., [136]	https://github.com/therneau/survival
R package survminer v0.4.9	Kassambra et al., [137]	https://rpkgs.datanovia.com/survminer/index.html
Other		
IDH1 and IDH2 pyrosequencing procedure	Radke et al., 2019[138]	N/A
IDH1 R132H immunohistochemistry procedure	Radke et al., 2019[138]	N/A
EPIC analyses procedure	Suwala et al., 2022[133]	N/A
iScan system	Illumina	Cat# SY-101-1001
Bead chip array platform	Illumina	Cat# 20028879
T10 basic Ultra-Turrax blender	IKA	0003737000
Bioruptor Plus	Diagenode	Cat# B01020001
Concentrator plus	Eppendorf	Cat# 5305000509
Nanodrop 2000	Thermo Scientific	Cat# ND-2000
AssayMAP Bravo	Agilent	Cat# G5571AA
EASY-nLC 1200	Thermo Fisher Scientific	Cat# LC140
Q Exactive HF	Thermo Fisher Scientific	Cat# 0726041
Q Exactive HF-X	Thermo Fisher Scientific	Cat# 0726042
Fused silica capillaries	Optronis GmbH	TSP 075 375
C18 beads for in-house packed chromatography columns	Dr.Maisch	ReproSil-Pur 120C18-AQ, 1.9 μm

RESOURCE AVAILABILITY

Lead contact

Further information and requests for resources and reagents should be directed to and will be fulfilled by the lead contact, Felix Meissner (felix.meissner@uni-bonn.de).

Materials availability

This study did not generate new unique reagents.

Data and code availability

- The mass spectrometry proteomics data have been deposited to the ProteomeXchange Consortium via the PRIDE partner repository and are publicly available as of the date of publication. Accession numbers are listed in the key resources table.
- The raw methylation data and the CNV profiles calculated from them have been deposited to the Gene Expression Omnibus – NCBI repository and are publicly available as of the date of publication. Accession numbers are listed in the key resources table.
- The paper does not report original code.
- Any additional information required to reanalyze the data reported in this paper is available from the lead contact upon request.

EXPERIMENTAL MODEL AND SUBJECT DETAILS

Human subjects

Formalin fixed paraffin embedded (FFPE) tumor samples were collected from patients who underwent surgery at the Department of Neurosurgery of the Charité, Universitätsmedizin Berlin, and diagnosed at the Department of Neuropathology Charité - Universitätsmedizin Berlin. The diagnoses were made according to the valid WHO classification for tumors of the CNS at the time of diagnosis (revised fourth edition, 2016) and re-evaluated when the WHO classification was updated (fifth edition 2021). Patients' ages at the time of surgery were 73 ± 7 years (mean ± SD) for IDHwt, 48 ± 10 years for codel, 36 ± 12 years for non-codel, and 39 ± 12 years for the CNS ctrl. The non-neoplastic CNS tissue samples originate from epilepsy patients whose temporal lobe has been resected because of mesial hippocampal sclerosis. Subsequently, the parahippocampal cortical and subcortical tissue was separated from the hippocampus and the white matter tissue in particular was used as controls. Further information can be found in Table S1. All IDH-mutant gliomas included in the study had IDH1 R132H mutations. This study was conducted according to the ethical principles of medical research involving human subjects according to the Declaration of Helsinki. The clinical data were assessed and anonymized for patients' confidentiality. Ethical approval (EA2/101/08) was granted by the institutional ethics board of the Charité Ethics Committee.

METHOD DETAILS

Clinical diagnostic procedures and sampling

IDH mutation status was determined by IDH1 R132H immunohistochemistry (IHC). In cases with unclear IDH immunohistochemistry results and in patients with glioblastomas under 55 years of age, an IDH1 and IDH2 pyrosequencing analysis was also performed.[138,139] The 1p/19q-codeletion status was determined using the EPIC methylation analysis – described below. As current diagnostic criteria for glioma include homozygous deletion of CDKN2A/B, this was inferred from the EPIC analysis later in the study.[15] IDHwt glioma exhibited frequent (8/11) loss of CDKN2A/B while only few (2/21) IDHmut glioma showed this. Similarly, EGFR amplification was common in IDHwt (5/11) but absent in IDHmut glioma. The tumor area was marked on an H&E section by a neuropathologist and the corresponding tissue was removed from the paraffin block for the proteome and molecular analyzes. Areas with high tumor cell content ($\geq$50%) were preferably chosen and adjacent sections from the tissue block macro-dissected for experiments. As gliomas are diffusely infiltrating tumors, three pronounced diffuse glioma samples with a tumor cell content of 35-50% were also included. For IDH-mutant samples, tumor content estimation was refined by categorization into solid tumor and infiltration zone.

DNA methylation and copy number variation analysis

For all tumors, DNA methylation and copy number analyses were performed using the EPIC (850k) Bead-Chip array platform (Illumina, USA).[133] All analyses were carried out according to the manufacturer's instructions. DNA was extracted from FFPE tumor samples using the Maxwell RSC FFPE Plus DNA Purification Kit (Promega, USA). After bisulfite conversion with the Zymo EZ Methylation Kit (Zymo Research Irvine, USA), the Infinium HD FFPE DNA Restore Kit was used for DNA restoration. The beadchips were scanned on the iScan system (Illumina USA).

Sample preparation for mass spectrometry

FFPE tumor samples were prepared for proteomic analysis as reported previously.[17] FFPE biobank specimens with an approximate 1.5 × 1 cm area were cut in 10μm slices with a microtome. Three slices were twice deparaffinized by 1mL of xylene at 50°C for 5min, washed twice with ethanol at RT for 5min and air-dried for 15min. Samples were homogenized in 300μL lysis solution (0.1M Tris/HCl, pH7.5, 10mM dithiothreitol) with an T10 basic Ultra-Turrax blender (IKA, Staufen, Germany). SDS was added to a final concentration of 4% w/v and sample homogenates were incubated at 99°C for 60 min at 600rpm on a Thermomixer (Eppendorf, Germany), cooled to RT, and sonicated on a Bioruptor Plus device for 15 cycles of 15s high power setting and 15s incubation (Diagenode SA, Belgium). After centrifugation for 10 min at 16 000 *g* at 4°C, proteins in the supernatant were alkylated with 55mM iodoacetamide for 30min in the dark and precipitated with 4-fold excess v/v of −20°C acetone overnight. The pellet was isolated by centrifugation at 16 000 *g* at 4°C for 10min, washed with 80%–20°C acetone, and resuspended in 100μL 8M urea aided by sonication as before.

The protein concentration was determined by BCA assay and proteins were digested with LysC for 3 hrs and subsequently diluted 3-fold with 50mM ammonium bicarbonate and digested with trypsin overnight. Digestions were performed at an enzyme:protein ratio of 1:50 w/w. Digestion was stopped by addition of trifluoroacetic (TFA) to 1% v/v and peptides were cleaned up according to the iST protocol using styroldivinylbenzol-reversed phase sulfonate material (SDB-RPS; Empore 3M, Germany) on in house-packed spin cartridges.[140] In brief, acidified peptides were loaded by centrifugation at 400*g*, washed twice with 200μL 1% v/v TFA in isopropanol, washed twice with 200μL 0.2% v/v TFA in water, eluted with 150μL 1% ammonia in 80% acetonitrile, and dried in a vacuum concentrator (Concentrator plus, Eppendorf, Germany). Peptides were then resuspended in 150 μL A* buffer (2% v/v acetonitrile, 0.1% v/v formic acid) aided by sonication and concentration was measured spectroscopically at 280nm (Nanodrop 2000, Thermo Scientific). One aliquot was kept for protein abundance 'total' proteomics while the bulk was used for phosphorylation site proteomics. For that purpose, 80μg of purified peptide were subjected to phosphopeptide enrichment using Fe(III)-NTA cartridges on the AssayMAP Bravo platform (Agilent, USA) according to the manufacturer's instructions. The eluate was dried and resuspended in 5 μL A* buffer.

Ultra-high pressure liquid chromatography and mass spectrometry

Samples were measured using an EASY-nLC 1200 (Thermo Fisher Scientific) coupled to a Q Exactive HF and a Q Exactive HF-X Orbitrap mass spectrometer (Thermo Fisher Scientific) in case of the proteome and phospho proteome samples, respectively. Purified peptides were separated on 50cm UHPLC columns with an inner diameter of 75μm packed in-house with ReproSil-Pur C18-AQ 1.9μm resin (Dr.Maisch GmbH) and ions were generated by a nano-electrospray ion source (Thermo Fisher Scientific). About 500ng of purified un-enriched peptides and the entire phosphopeptide enrichment eluate per sample corresponding to less than 500ng were loaded on the liquid chromatography column. Un-enriched peptides were eluted at a flow rate of 250 nL/min and a temperature of 60°C over a 160min gradient with decreasing concentration of buffer A (0.1% v/v formic acid in water) and concomitantly increasing concentration of buffer B (0.1% v/v formic acid, 80% v/v acetonitrile). The gradient used for separation of un-enriched peptides started at 2% v/v B, followed by several phases of linear increases to 5% at minute 3, to 25% at minute 109, to 35% at minute 136, to 60% at minute 148, to 95% at minute 151, a plateau at 95% up to minute 154, a decrease to 5% reached at minute 157 and further plateau at 5% until minute 160. Phosphopeptide-enriched samples were separated by a gradient starting at 3% B, followed by linear increases to 19% at minute 60, to 41% at minute 90, to 90% at minute 95, and a plateau at 90% until minute 100 at a flow of 300 nL/min at 60°C.

Generally, the mass spectrometers were operated by the Xcalibur software (Thermo Fisher) and MS/MS data were recorded in the data-dependent acquisition (DDA) mode. Survey scan (MS1) settings included an ion target value of 3×10^6 charges in the 300–1650 *m/z* range with a maximum injection time of 25 ms and a resolution of 60,000 at *m/z* 200. For non-enriched peptides, up to 15 MS/MS spectra with an ion target value of 10^5 charges, a maximum injection time of 25 ms, a resolution of 15,000 at *m/z* 200, a 1.4 *m/z* precursor isolation window, and a 20s dynamic exclusion list were recorded per DDA cycle. For phospho-enriched peptides, up to 10 MS/MS spectra were acquired per cycle with identical parameters but a maximum injection time of 50ms, a 1.6 *m/z* isolation window, and a dynamic exclusion window of 30 s. Precursors ions with charges other than 2-5 were not selected for MS/MS events. Fragmentation was performed by higher-energy C-trap dissociation (HCD) with a normalized collision energy of 27eV.

QUANTIFICATION AND STATISTICAL ANALYSIS

DNA methylation and copy number variation data analysis

DNA based classification was performed for 850k data using the publicly available "brain tumor classifier", version v11b4, ref. [14]. One oligodendroglioma sample with 1p/19q codeletion confirmed by EPIC analyses was surprisingly assigned 'high grade astrocytoma' by this algorithm. We thus reanalyzed this sample with the recently improved classifier version v12.5[133] which assigned the new class 'oligosarcoma' to this sample in line with its oligodendroglial origin.

Copy number variations were calculated from IDAT files using the R/Bioconductor conumee package, and were visualized using ComplexHeatmaps v2.10.0. The Integrative Genomics Viewer (IGV) was used to assess chromosomal gains and losses considering the tumor cell content.[134,135,141] In general, changes were considered potentially relevant if the intensity ratio of a segment deviation from the baseline by more than 0.1, ref. [14]. In addition, we made summary copy number profiles for both IDH mutated groups (A and B). This analysis was done using an adaption of the conumee script (provided by Dr. Damian Stichel, Neuropathology Heidelberg). This algorithm allowed determining CNV load (CNV-L) for each tumor, resulting in a split for a value of 349.695.798 base pairs.[15] This CNV load refers to the sum of all gains and deletions as determined by analysis of the 850k raw data by our performed algorithm.

Progression-free survival analysis

Outcome data were available in 20 of 21 IDHmut A/B patients. Progression free survival analysis was performed using the R v4.1.1 packages survival v3.1-8 and survminer v0.9.9, ref. [136] and [137]. We used Kaplan-Meier estimates to investigate differences in progression free survival. The starting point for the analysis of the results was the date of the first histological diagnosis of a glioma. As an "event" for progression analysis, we defined either the performance of another surgical intervention (using the date of surgery as event date) or if available tumor progression on MRI (using the date of the MRI as event date). No patients died during follow up period. Median follow up time was 6.5 years (range 1 year–14 years).

Mass spectrometry data processing

To process MS raw files, we employed the MaxQuant software versions 1.5.8.4 and 1.6.0.15 for the un-enriched peptides and phospho-enriched peptides, respectively.[131] Spectra were searched against the UniProtKB human FASTA database of canonical and isoform protein sequences downloaded in March 2018 and comprising 93,786 entries. Default search parameters were utilized unless stated differently. In brief, tryptic peptides with a minimum length of 7 amino acids, a maximum mass of 4600 Da, and two miscleavages at maximum were searched. Carbamidomethlyation was set as a fixed modification and methionine oxidation and protein N-terminal acetylation as variable modifications, for the search of phospho-enriched peptides phosphorylation of serine, threonine and tyrosine was additionally included. A maximum of five modifications per peptide was permitted. A false discovery rate (FDR) cutoff of 1% was applied at the peptide and protein level. The search feature "Match between runs," which allows the transfer of peptide identifications in the absence of MS/MS-based identification after nonlinear retention time alignment was enabled with a maximum retention time window of 0.7 min. Protein abundances were normalized with the MaxLFQ label-free normalization algorithm incorporated in MaxQuant.

Data preprocessing and bioinformatic analysis

Data analysis was mainly performed in the Perseus environment version 1.6.1.3 and in version 1.6.0.9 for correlation analysis.[132] Potential contaminants, proteins only identified by site, and search decoys were excluded from further analysis. Protein abundance was log_2-transformed and proteins that were not quantified in at least seven samples of at least one of the three WHO entities and one ctrl (IDHwt, IDHmut, 1p/19q-codel, ctrl CNS) were removed. Missing values for protein abundances were imputed according to Perseus default settings from normal distributions around the detection limit with a SD of 0.3 times that of the observed protein distribution of that sample and a downshift of 1.8 standard deviations. Volcano plots were generated in Perseus and FDR-controlled by q-value calculation using a permutation strategy in conjunction with a SAM-statistic with an s0-parameter of 0.1.[142] Proteins above the cutoff line are significant according to q-value <5%. Bar plots and boxplots with boxes and whiskers depicting the inter-quartile and minimum to maximum range, respectively, were created in GraphPad Prism 9. T-tests with Welch's correction were used for group comparisons in these plots. Significance levels were $p < 0.05$, <0.01, <0.001, and <0.0001 indicated by one to four stars. Heat maps and hierarchical clusters were generated in Perseus. Protein intensities were Z-Scored or normalized by subtraction of the median intensity across samples as stated in the figure legends. In case of sample groups, mean group intensities were used. Principal component analysis, Pearson correlation analysis, and one-way ANOVA with s0 parameter-modified test statistic were performed using Perseus tools. Analysis of ATRX-correlating proteins was limited to IDHmut tumor samples as ATRX loss is mostly restricted to IDHmut gliomas.[143]

Phosphoproteome-specific analysis

For phosphosite analysis, the phospho (STY) site table generated by MaxQuant containing multiplicity-level quantification was transformed to phosphosite-level quantification by the Perseus expand site table feature. Like protein data, phosphosite abundances were log_2-transformed and filtered for seven quantifications. Moreover, phosphosites were filtered for high localization confidence ($p > 0.75$), termed class I sites, and the median phosphosite intensity of each sample was subtracted from all phosphosites within that sample. Subsequently, missing values were imputed as above.

For the analysis of the glycolysis enzyme phosphorylation signature, phosphosite abundances were normalized to their matching protein abundance for each sample. To avoid amplification of error due to missing values and imputation on both protein and phosphopeptide level, unimputed protein intensities were subtracted from unimputed phosphosite intensities in log_2-space, equivalent to division in linear space. Subsequently, the median was subtracted within samples, normalized phosphosites filtered for at least seven quantifications in at least one of the WHO sample groups and imputation performed as above.

Proteome annotations, chromosomal analysis, and survival associations

Proteins were annotated via the in-built Perseus function with gene ontology terms for biological processes (GOBP), cellular compartments (GOCC), molecular function (GOMF), UniProt Keywords, UniProt protein families, UniProt protein-protein interactions ('interacts with'), and genomic information including chromosomal and base pair position.

Chromosome arm area abundances were calculated as mean abundance of all proteins with corresponding chromosomal position and normalized by subtracting the median abundance within samples. For heatmap visualization, the median abundance within proteins across samples was subtracted. Genome assembly issues and the Y chromosome for which only one protein was quantified were excluded.

Annotation term enrichment on the PCA loadings, i.e. protein contributions, to the two main principal components was performed with the 2D enrichment tool in Perseus.[144] Annotations with a Benjamini-Hochberg-adjusted q-value higher than 0.5% and or less than 5 proteins were excluded. Remaining annotations were manually assigned to the meta-categories such as 'chromatin'.

For analysis of functional metabolic groups of proteins, proteins were selected according to the terms 'glycolysis' (UniProt Keywords) and 'tricarboxylic acid cycle' (UniProt Keywords), and the terms for 'mitochondrial respirator chain complex' I-IV (GOCC), respectively, and 'mitochondrial proton-transporting ATP synthase complex' as complex V (GOCC). Tumor suppressors and oncoproteins were filtered according to UniProt Keywords annotation for 'tumor suppressor genes' and 'proto-oncogenes'.

Survival associations mapped onto outlier proteins regulated on chr. 10, chr. 7, and arms 1p and 19q derived from TCGA glioma Affymetrix human exon 1.0 ST transcriptomics data accessed via betastasis (http://www.betastasis.com). High and low expression were separated by the median expression value. Significance of association calculated by the log -rank test were taken from betastasis.

Tumor content analyses

Various controls were performed to check for potential associations of the proteome-based sub-stratification of IDHmut tumors with clinical parameters or tumor content (see supplemental information). For stratifications into 'high' and 'low' groups for parameters, e.g. solid tumor content, sample assignment was made in the way entailing maximum parameter separation while maintaining balanced composition of the two groups regarding HGG-IDHmut-B and HGG-IDHmut-A. Regression analysis was performed using the lm() linear model in R version 3.6.3, fitting protein abundances based on HGG-IDHmut-A/B status, 1p/19q codeletion status, and two tumor content variables (i: solid tumor area, and ii: infiltration zone area) among IDHmut samples.

Further, proteome differences were compared to cell type differences between isolated astrocytes and neurons using available murine proteomics data.[130] Proteins were matched based on identical gene names. Mouse cell data were filtered for astrocytes

(n = 3), oligodendrocytes at DIV4 (n = 3), neurons at DIV15, and adult microglia (n = 3). Similar to our proteome data, proteins without at least two out of three quantifications in at least one cell type were removed and subsequently missing values were imputed as above.

Integration with other glioma proteome datasets

Proteome differences between HGG-IDHmut-A and B were compared to published glioma proteome data.[25,119,120] The CPTAC/Wang dataset stratified glioma samples by a multi-omics-defined phenotype: 29 nmf1/proneural-like, 37 nmf2/mesenchymal-like, 26 nmf3/classical-like, 6 IDH mutant (IDH1 R132H), and 10 non-neoplastic ctrl CNS. One sample with a non-hotspot IDH-mutation (R222C) in the CPTAC dataset, assigned to nmf3/classical-like, was excluded. The dataset was further filtered for proteins with at least 70% observations in at least 1 'multi-omic' group reducing the dataset from 10,998 to 10,206 proteins. Remaining missing values were imputed analogously as in our dataset. A list of the human proteome with RefSeq and UniProt IDs for each protein was downloaded from UniProt to match proteins identified by RefSeq ID in the CPTAC dataset to proteins specified by UniProt IDs in our dataset, 5195 proteins overlapped. The Oh et al. study comprised 26 GPC1 (GBM proteomic cluster 1, high glycolysis) subtype and 13 GPC2 (high oxidative phosphorylation) subtype IDHwt glioblastoma samples, which were used in their main GPC1/GPC2 clustering and the re-analysis in our study. The proteome dataset contained 3909 proteins without missing values. Proteins were specified by UniProt IDs which we used to match proteins to our data, 3715 proteins overlapped. The Wong dataset comprised 6 control CNS samples, 21 IDH-mutant 1p/19q-codeleted (Wong et al.: 'type I'), 17 IDH-mutant 1p/19q non-codeleted ('type II'), 10 IDH-wt ('type III') glioma samples and additional reference samples which we removed from further analysis. The dataset comprising 7988 protein groups was filtered for proteins present in all samples reducing the number to 5897 proteins. Proteins were matched to our dataset based on UniProt IDs. Our hierarchical clustering classified the IDHmut glioma into 10 IDHmut-A (comprising 6 'type I' and 4 'type II') and 28 IDHmut-B (comprising 15 'type I' and 13 'type II').

Cell Reports Medicine, Volume *4*

Supplemental information

Proteomics separates adult-type diffuse high-grade gliomas in metabolic subgroups independent of 1p/19q codeletion and across IDH mutational status

Jakob Maximilian Bader, Nikolaus Deigendesch, Martin Misch, Matthias Mann, Arend Koch, and Felix Meissner

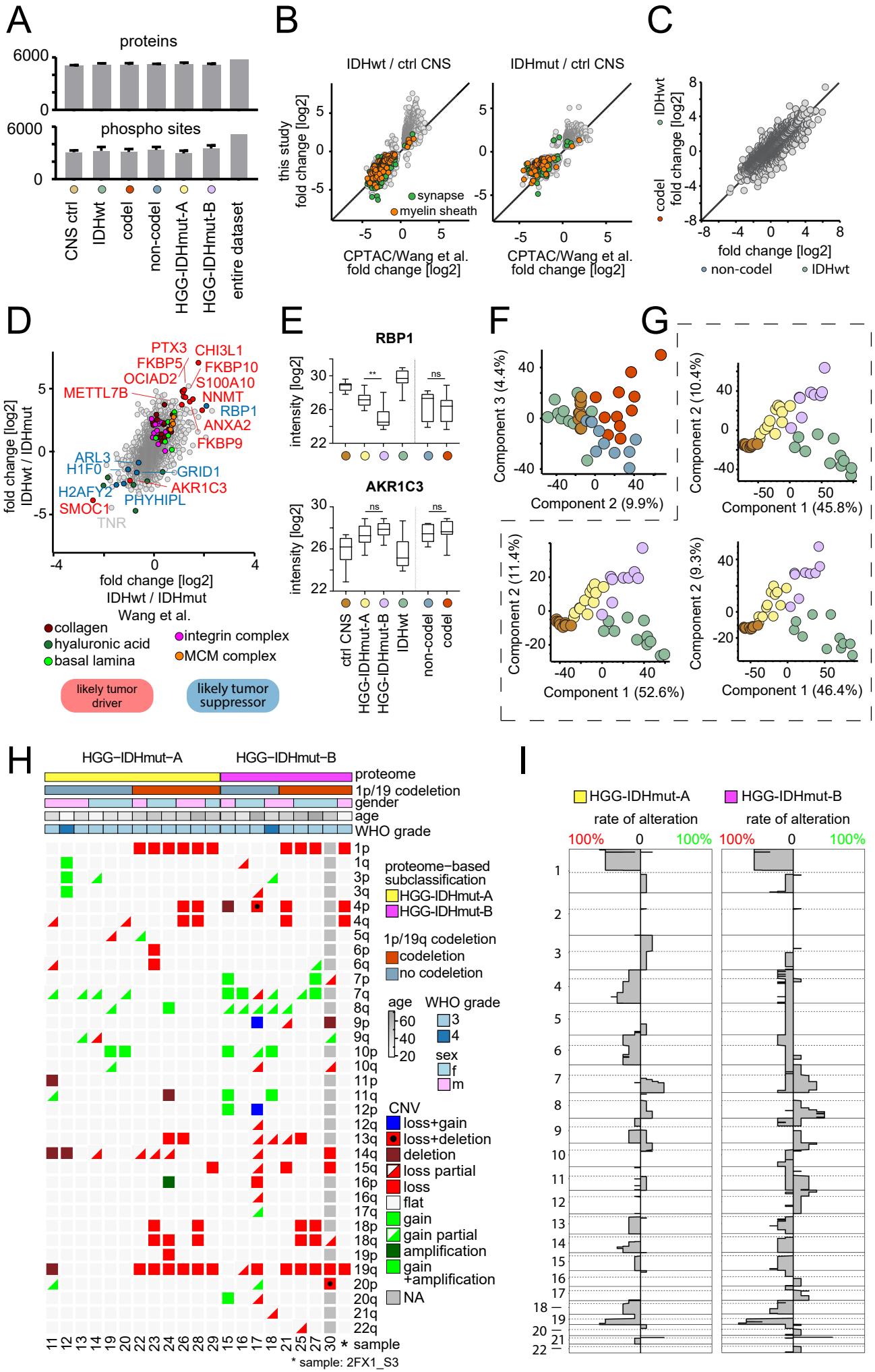
A
proteins
6000
0
phospho sites
6000
0
CNS ctrl
IDHwt
codel
non-codel
HGG-IDHmut-A
HGG-IDHmut-B
entire dataset
B
IDHwt / ctrl CNS
IDHmut / ctrl CNS
this study fold change [log2]
synapse
myelin sheath
CPTAC/Wang et al. fold change [log2]
C
IDHwt
codel
fold change [log2]
non-codel
IDHwt
D
PTX3
CHI3L1
FKBP5
FKBP10
OCIAD2
S100A10
METTL7B
NNMT
RBP1
ANXA2
FKBP9
ARL3
H1F0
GRID1
H2AFY2
AKR1C3
PHYHIPL
SMOC1
TNR
fold change [log2] IDHwt / IDHmut
fold change [log2] IDHwt / IDHmut Wang et al.
collagen
hyaluronic acid
basal lamina
integrin complex
MCM complex
likely tumor driver
likely tumor suppressor
E
RBP1
AKR1C3
intensity [log2]
ctrl CNS
HGG-IDHmut-A
HGG-IDHmut-B
IDHwt
non-codel
codel
F
Component 3 (4.4%)
Component 2 (9.9%)
Component 2 (10.4%)
Component 1 (45.8%)
Component 2 (11.4%)
Component 1 (52.6%)
Component 2 (9.3%)
Component 1 (46.4%)
G
H
HGG−IDHmut−A
HGG−IDHmut−B
proteome
1p/19 codeletion
gender
age
WHO grade
proteome−based subclassification
HGG-IDHmut-A
HGG-IDHmut-B
1p/19q codeletion
codeletion
no codeletion
age
WHO grade
sex
CNV
loss+gain
loss+deletion
deletion
loss partial
loss
flat
gain
gain partial
amplification
gain +amplification
NA
* sample
* sample: 2FX1_S3
I
HGG-IDHmut-A
HGG-IDHmut-B
rate of alteration
100%
0
100%

Figure S1. Overall dataset, separation glioma subgroups and comparison to CPTAC/Wang et al. dataset. Related to Figure 1.

A) Number of quantified proteins and high-confidence class I (localization probability > 0.75) phosphor-sites in filtered dataset. Samples, n=10 (ctrl CNS), n=12 (HGG-IDHmut-A), n=9 (HGG-IDHmut-B), n=11 (IDHwt), n=11 (codel), n=10 (non-codel).

B) Comparison of CPTAC/Wang et al. glioma proteome data to our glioma dataset. Specifically, comparison of IDHwt to ctrl CNS protein fold changes [log2] (left) and IDHmut to ctrl CNS protein fold changes [log2] right. Entities nmf1, nmf2, nmf3 in CPTAC dataset are IDHwt. Only proteins significantly regulated (q < 5%) in at least one dataset included: 2732 (IDHwt vs ctrl CNS) and 1351 (IDHmut vs ctrl CNS). Consistency of regulation: 99% concordance and Pearson r = 0.92 (IDHwt vs ctrl CNS) and 98% concordance and Pearson r = 0.91 (IDHmut vs ctrl CNS). Samples, this study: n=10 (ctrl CNS), n=11 (IDHwt), Wang et al.: n=10 (ctrl CNS), n=91 (IDHwt).

C) IDHwt/IDHmut proteome differences depending on 1p/19q-codeletion status of IDHmut. Samples as in A.

D) Comparison of IDHwt/IDHmut differences between datasets of this study (y axis) and CPTAC (x axis). Entities nmf1, nmf2, nmf3 in CPTAC/Wang et al. dataset are IDHwt. All proteins overlapping in both datasets (5241) shown, Pearson r = 0.57. Filtering for proteins significantly regulated (q < 5%) in both datasets, increases correlation to Pearson r = 0.89 (701 proteins). Outlier proteins and proteins belonging to enriched annotation terms of interest as in Fig. 1E highlighted. Samples, this study: n=21 (IDHmut), n=10 (IDHwt), CPTAC/Wang: n=6 (IDHmut), n=91 (IDHwt).

E) Abundances of RBP1 and AKR1C3 across sample groups of this study. Samples as in A.

F) Separation of codeleted and non-codeleted IDH-mutant samples in the combined second and third components of the principal component analysis of the glioma proteome. Green IDHwt, brown ctrl CNS, red 1p/19q-codeleted IDH-mutant, blue non-1p/19q-codeleted samples. Samples as in A.

G) Equivalence of the HGG-IDHmut-A / HGG-IDHmut-B subgroup clustering in differently filtered datasets. PCA analysis of dataset comprising ANOVA-significant (q < 5%) proteins (top right, 3749 proteins), dataset comprising proteins quantified in all 42 samples without missing values (bottom left, 2625 proteins), and dataset comprising the top 25% most variable proteins with highest CVs across all 42 samples (bottom right, 1439 proteins). Samples as in A.

H) CNV profiles across samples. Samples as in A.

I) CNV load plots as averages within the groups of HGG-IDHmut-A and HGG-IDHmut-B. Amplifications highlighted as alterations in green to the right, deletions as alterations in red to the left. Samples as in A.

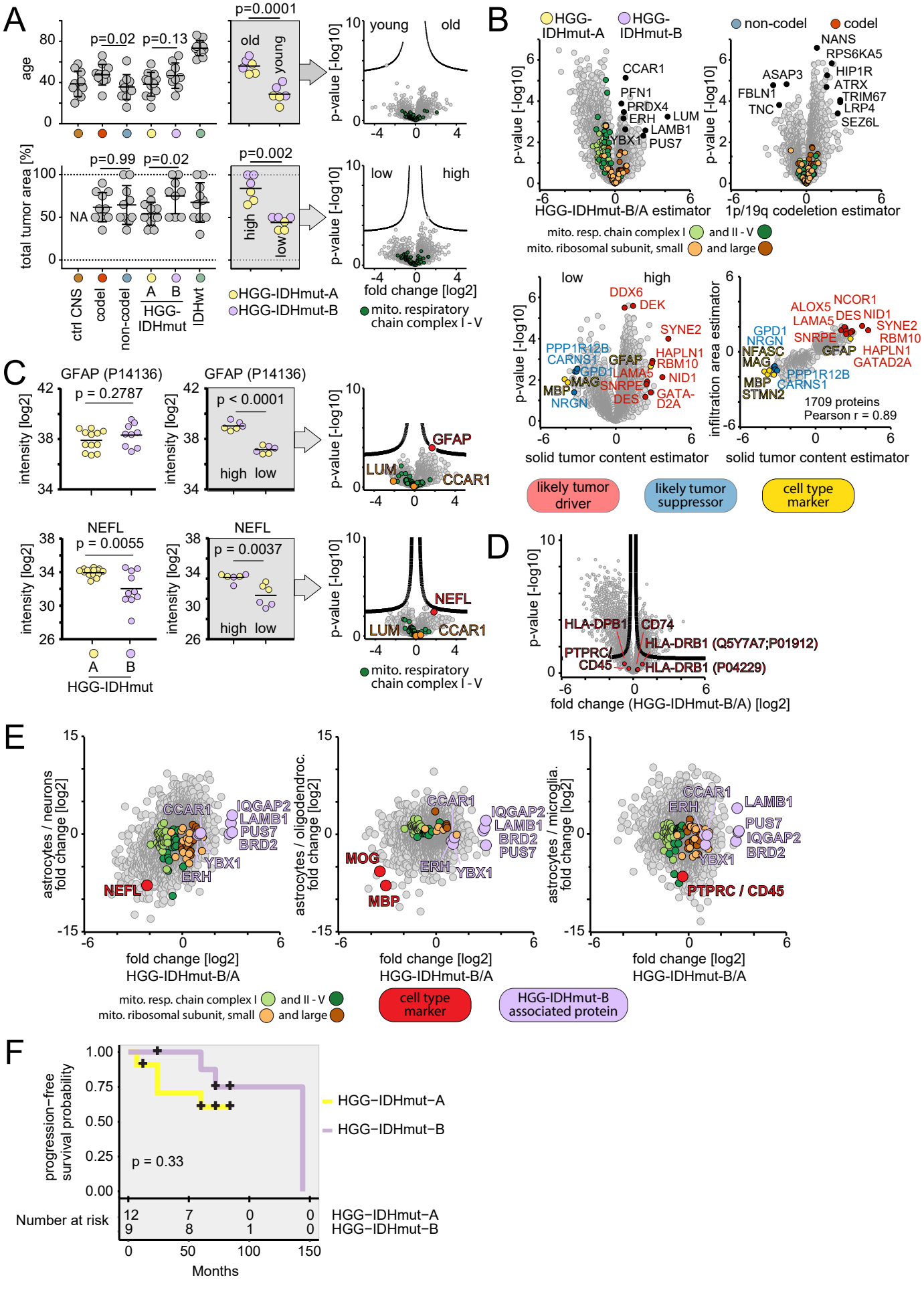
A
age
p=0.02
p=0.13
p=0.0001
old
young
p-value [-log10]
young
old
total tumor area [%]
p=0.99
p=0.02
p=0.002
high
low
NA
fold change [log2]
ctrl CNS
codel
non-codel
A
B
HGG-IDHmut
IDHwt
HGG-IDHmut-A
HGG-IDHmut-B
mito. respiratory chain complex I - V
B
HGG-IDHmut-A
HGG-IDHmut-B
CCAR1
PFN1
PRDX4
ERH
LUM
LAMB1
YBX1
PUS7
HGG-IDHmut-B/A estimator
non-codel
codel
NANS
RPS6KA5
HIP1R
ATRX
TRIM67
LRP4
SEZ6L
ASAP3
FBLN1
TNC
1p/19q codeletion estimator
mito. resp. chain complex I and II - V
mito. ribosomal subunit, small and large
low
high
DDX6
DEK
SYNE2
PPP1R12B
CARNS1
GFAP
HAPLN1
RBM10
GPD1
LAMA5
NID1
MAG
SNRPE
MBP
NRGN
DES
GATA-D2A
solid tumor content estimator
ALOX5
NCOR1
LAMA5
DES
NID1
SYNE2
GPD1
NRGN
SNRPE
RBM10
NFASC
GFAP
HAPLN1
MAG
GATAD2A
PPP1R12B
CARNS1
MBP
STMN2
infiltration area estimator
1709 proteins
Pearson r = 0.89
likely tumor driver
likely tumor suppressor
cell type marker
C
GFAP (P14136)
p = 0.2787
p < 0.0001
intensity [log2]
high low
GFAP
LUM
CCAR1
NEFL
p = 0.0055
p = 0.0037
A
B
HGG-IDHmut
mito. respiratory chain complex I - V
D
p-value [-log10]
HLA-DPB1
CD74
PTPRC/ CD45
HLA-DRB1 (Q5Y7A7;P01912)
HLA-DRB1 (P04229)
fold change (HGG-IDHmut-B/A) [log2]
E
astrocytes / neurons fold change [log2]
astrocytes / oligodendroc. fold change [log2]
astrocytes / microglia. fold change [log2]
CCAR1
IQGAP2
LAMB1
PUS7
BRD2
YBX1
ERH
NEFL
MOG
MBP
PTPRC / CD45
fold change [log2] HGG-IDHmut-B/A
mito. resp. chain complex I and II - V
mito. ribosomal subunit, small and large
cell type marker
HGG-IDHmut-B associated protein
F
progression-free survival probability
p = 0.33
HGG−IDHmut−A
HGG−IDHmut−B
Number at risk
12 7 0 0
9 8 1 0
Months

Figure S2. Analysis of HGG-IDHmut-A/B association with patient demographics, survival and tumor content. Related to Figure 1.

Upon identification of the proteome-based classification, we aimed to link this classification to patient's demographic data or histological correlates.

- **A)** Influence of patient age (top row) and tumor content (bottom row) on HGG-IDHmut-A/B separation. Left: Distribution of values (top: patient age at diagnosis, bottom: area % of sample that is tumor according to histopathological assessment) across sample groups of this study. Samples, n=10 (ctrl CNS), n=12 (HGG-IDHmut-A), n=9 (HGG-IDHmut-B), n=11 (IDHwt), n=11 (codel), n=10 (non-codel). Center: Stratification of control groups (n=6 in each group) for age (top) and tumor content (bottom), balanced for HGG-IDHmut-A and B composition, respectively. Right: Proteome differences between stratified control groups, mitochondrial respiratory chain proteins highlighted. A neuropathologist did not identify discerning histomorphological features, but estimated the fractions of the tissue section occupied by the solid tumor, the tumor infiltration zone, and the reactive CNS tissue for further analysis. Moderately higher total tumor area (solid + infiltration) in HGG-IDHmut-B comparted to A. However, no significant proteome differences between groups of samples stratified into 'high tumor area' and a 'low tumor area' for total tumor area, (and likewise for solid or infiltration area, not shown).
- **B)** Linkage of differential tumor content to independent cancer drivers but not the HGG-IDHmut-A/B separation. Linear regression model predicting protein intensity based on variables HGG-IDHmut-A/B status, 1p/19q codeletion status, solid tumor content, tumor infiltration area. Regression results showing estimators (x axis) for HGG-IDHmut-A/B status (top left), 1p/19q codeletion status (top right), solid tumor content (bottom left), and their significance (y axis), respectively. Correlation of estimators for solid tumor area and tumor infiltration area (bottom right) for proteins significant ($p <$ 5%) in at least one tumor area dimension. Proteins of interest highlighted including mitochondrial proteins (top row) and tumor suppressor, oncoproteins, and cell type markers (bottom row). Samples, n=12 (HGG-IDHmut-A), n=9 (HGG-IDHmut-B), n=11 (codel), n=10 (non-codel). Main features of HGG-IDHmut-A/B separation (mito. resp. chain complex signature, outlier proteins) confirmed, and 1p/19q codel-associated protein regulation preserved and statistically more significant, after correction for covariates by regression model. Outlier proteins associated with solid or infiltration tumor area distinct to the proteins linked to either subgrouping (HGG-IDHmut-A/B or 1p/19q status) but protein association with the two tumor area parameters highly correlated. Many high tumor content-associated proteins previously implicated as oncogenes, predominantly in other cancer types, including NID1, SYNE2, DEK, DDX6, DES, GATAD2A, SNRPE, ALOX5, HAPLN1, LAMA5, NCOR1, and RBM10[145-157]. Conversely, low tumor content proteins comprising functional CNS proteins such as myelin (MBP, MAG) and neuronal proteins (NFASC, STMN2), and tumor suppressors (NRGN, CARNS1, GPD1[158-160]).
- C) Relationship of HGG-IDHmut-A/B separation and differential content of astrocyte and neuron content. Sample numbers as in B. Left: Distribution of values (top: GFAP intensity, bottom: NEFL intensity) across sample groups of this study. Center: Stratification of control groups (n=6 in each group) for GFAP intensity (top) and NEFL intensity (bottom) balanced for HGG-IDHmut-A and B composition, balanced for HGG-IDHmut-A and B composition, respectively. Right: Proteome differences between stratified control groups, mitochondrial respiratory chain proteins and proteins of interest highlighted. No significant proteome alterations or differences of mitochondrial respiratory chain proteins as in HGG-IDHmut-A/HGG-IDHmut-B comparison in these stratifications.
- D) Apparent non-regulation of microglia-associated proteins between HGG-IDHmut-A (n=12) and B (n=9) proteome.
- E) Comparison of proteome differences between HGG-IDHmut-A / B sample groups and differences between isolated astrocytes and neurons (left), astrocytes and oligodendrocytes (center), and astrocytes and microglia (right) accessible for mouse[144]. No correlation of mitochondrial protein abundance differences between the HGG-IDHmut-A/B subtypes with the abundance differences between isolated brain cell types. Proteins with q-value of 5% or lower in at least one of the two dimensions each (cell types, glioma subtypes) included. Neuronal (NEFL), oligodendroglial (MOG, MBP) and microglial marker proteins (PTPRC/CD45) labelled in red. Outlier proteins associated with HGG-IDHmut-B labelled in pink. Mitochondrial respiratory chain proteins green and mitochondrial ribosomal proteins brown. Respiratory chain complex V refers to ATP synthase. Pearson correlation coefficients for all

proteins, left: r = 0.41, center: r = 0.09, right: r = -0.12 and for labelled mitochondrial proteins, left: r = -0.04, center: r = -0.03, right: r = -0.08. Samples, n= 12 (HGG-IDHmut-A), n=9 (HGG-IDHmut-B), n=3 (astrocytes), n=3 (oligodendrocytes DIV4), n=3 (neurons DIV15), n=3 (adult microglia).

F) Progression-free survival of HGG-IDHmut-A (n=12) and HGG-IDHmut-B (n=9).

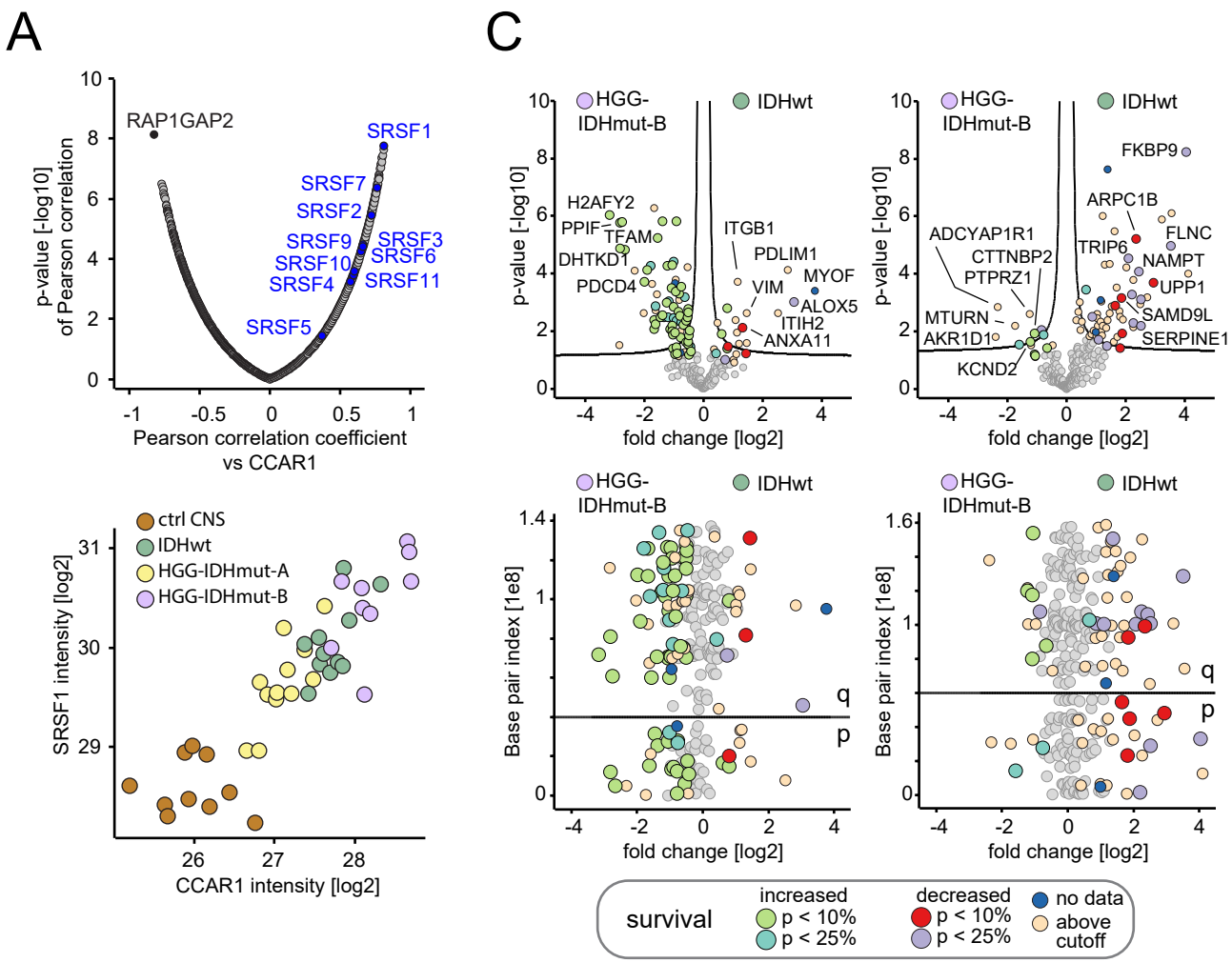
A
RAP1GAP2
SRSF1
SRSF7
SRSF2
SRSF9
SRSF3
SRSF10
SRSF6
SRSF4
SRSF11
SRSF5
p-value [-log10] of Pearson correlation
Pearson correlation coefficient vs CCAR1
ctrl CNS
IDHwt
HGG-IDHmut-A
HGG-IDHmut-B
SRSF1 intensity [log2]
CCAR1 intensity [log2]
C
HGG-IDHmut-B
IDHwt
H2AFY2
PPIF
TFAM
DHTKD1
PDCD4
ITGB1
PDLIM1
MYOF
VIM
ALOX5
ITIH2
ANXA11
FKBP9
ARPC1B
ADCYAP1R1
FLNC
TRIP6
CTTNBP2
NAMPT
PTPRZ1
UPP1
MTURN
SAMD9L
AKR1D1
SERPINE1
KCND2
p-value [-log10]
fold change [log2]
Base pair index [1e8]
q
p
survival
increased
p < 10%
p < 25%
decreased
p < 10%
p < 25%
no data
above cutoff
B
nuclear telomere cap complex
G-rich strand telomeric DNA binding
telomerase RNA binding
telomere maintenance via telomerase
19q arm
1p arm
rank
annotation enrichment score in Pearson coeffiecient for ATRX-correlation
GGH
CTSD
GMPS
NANS
RPA1
XRCC6
TERF2
RAD50
HNRNPU
TERF2IP
GAR1
XRCC5
HSP90AB1
HNRNPA2B1
MRE11A
SNRPB
DKC1
HNRNPC
DHX36
HNRNPA1
NHP2
SNRPD3
HSP90AA1
HNRNPC
PTGES3
RPA2
PARN
EXOSC10
TNKS1BP1
p-value [-log10] of Pearson correlation
Pearson correlation coefficient vs ATRX
D
chromosome arm 1p
chromosome arm 19q
non-codel
codel
LRRC40
MANEAL
PKN2
ATPIF1
p-value [-log10]
fold change [log2]
Base pair index [1e8]
p
q

Figure S3: CCAR1 and ATRX correlation analysis, survival association of regulated chr. 7, chr. 10, and 1p/19q proteins. Related to Figure 2.

A) CCAR1 correlation analysis. Top: Proteins correlating to CCAR1 across all 32 tumor samples. Bottom: Abundances of CCAR1 and SRSF1 across all samples of dataset. Pearson coefficient r = 0.89. Sample groups color-coded, brown control CNS, green IDHwt, yellow HGG-IDHmut-A, pink HGG-IDHmut-B.

B) ATRX correlation analysis. Top: Annotations enriched in proteins with extreme (high/low) Pearson correlation coefficients vs ATRX according to Perseus 1D annotation enrichment. IDHmut tumors (n=21) included. 1p/19q affiliation of proteins treated as annotation for enrichment analysis. Bottom: roteins correlating to ATRX across IDHmut tumors. Proteins annotated with telomerase-related terms color-coded (terms of top panel). Proteins linked to more than one term assigned color code of term with fewest proteins.

C) Survival association of chromosome 10 (left) and chromosome 7 (right) proteins regulated between IDHwt (n=11) and HGG-IDHmut-B (n=9). Select outlier proteins are colored based on the association of their transcripts with survival in the TCGA (The Cancer Genome Atlas) study. Top: Regulation. Bottom: Relationship between differential abundance and genomic position of proteins encoded on chromosome 10 (left) or chromosome 7 (right).

D) Survival association of chromosome arm 1p (left) and 19q (right) proteins regulated between codel (n=11) and non-codel IDHmut (n=10). Select outlier proteins are colored based on the association of their transcripts with survival in the TCGA (The Cancer Genome Atlas) study. Top: Regulation. Bottom: Relationship between differential abundance and genomic position of proteins encoded on chromosome arm 1p (left) or chromosome arm 19q (right).

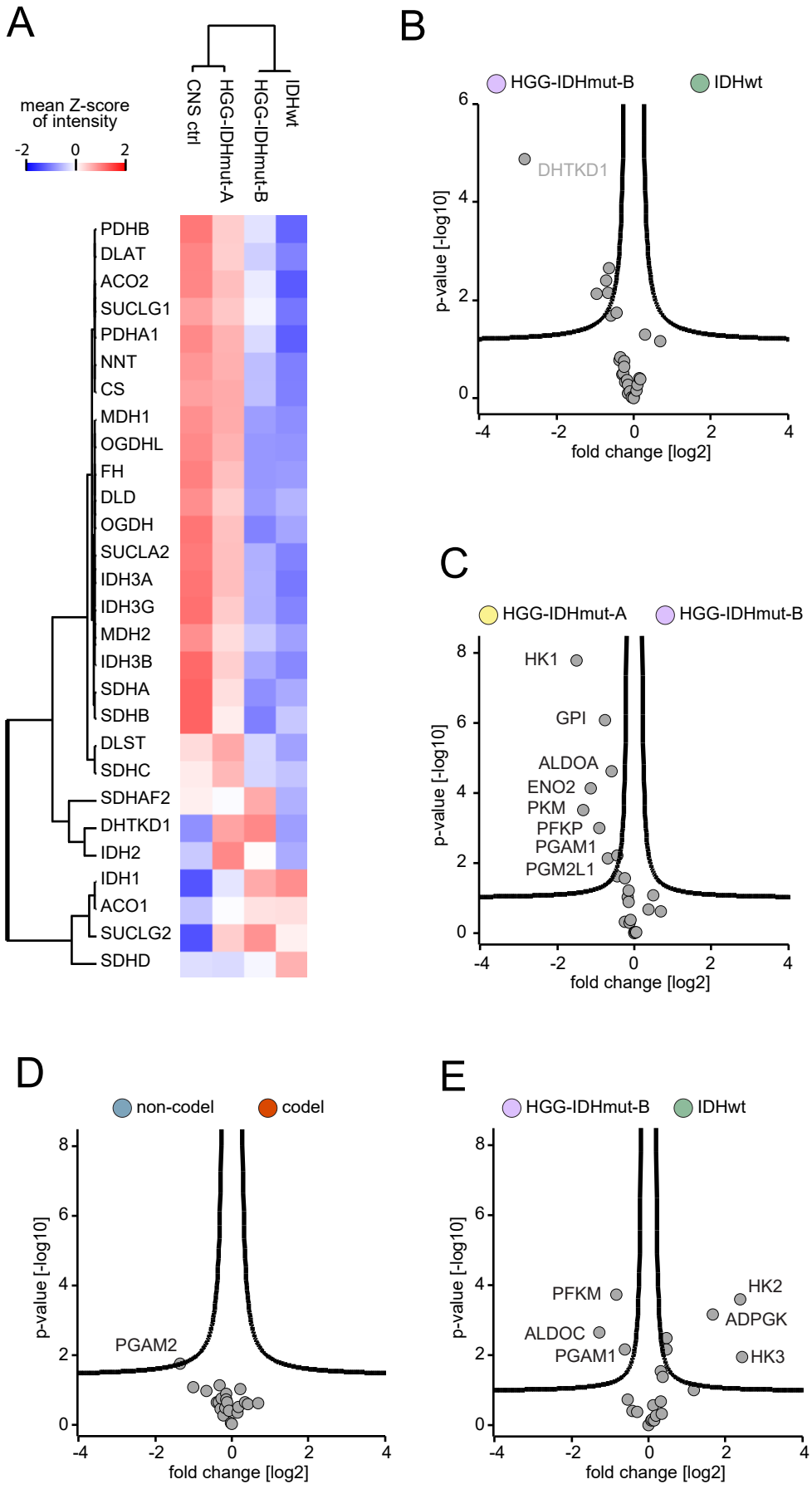
A
mean Z-score of intensity
-2
0
2
CNS ctrl
HGG-IDHmut-A
HGG-IDHmut-B
IDHwt
PDHB
DLAT
ACO2
SUCLG1
PDHA1
NNT
CS
MDH1
OGDHL
FH
DLD
OGDH
SUCLA2
IDH3A
IDH3G
MDH2
IDH3B
SDHA
SDHB
DLST
SDHC
SDHAF2
DHTKD1
IDH2
IDH1
ACO1
SUCLG2
SDHD
B
HGG-IDHmut-B
IDHwt
DHTKD1
p-value [-log10]
fold change [log2]
C
HGG-IDHmut-A
HGG-IDHmut-B
HK1
GPI
ALDOA
ENO2
PKM
PFKP
PGAM1
PGM2L1
p-value [-log10]
fold change [log2]
D
non-codel
codel
PGAM2
p-value [-log10]
fold change [log2]
E
HGG-IDHmut-B
IDHwt
PFKM
ALDOC
PGAM1
HK2
ADPGK
HK3
p-value [-log10]
fold change [log2]

Figure S4. Tricarboxylic acid cycle and glycolysis. Related to Figure 3.

A) Abundance of tricarboxylic acid cycle proteins across alternatively-defined entities of this study. Clustering associates the HGG-IDHmut-B sample group with IDHwt and HGG-IDHmut-A with ctrl CNS. Abundance as sample group mean of cross-sample Z-Scored intensity. Samples, n=10 (ctrl CNS), n=11 (IDHwt), n=11 (codel), n=10 (non-codel).

B) Regulation of tricarboxylic acid cycle proteins between IDHwt (n=11) and HGG-IDHmut-B (n=9).

C-E) Regulation of glycolysis proteins between HGG-IDHmut-B and HGG-IDHmut-A (C), codel and non-codel (D), and IDHwt and HGG-IDHmut-B (E). Samples, n=12 (HGG-IDHmut-A), n=9 (HGG-IDHmut-B), n=11 (IDHwt), n=11 (codel), n=10 (non-codel).

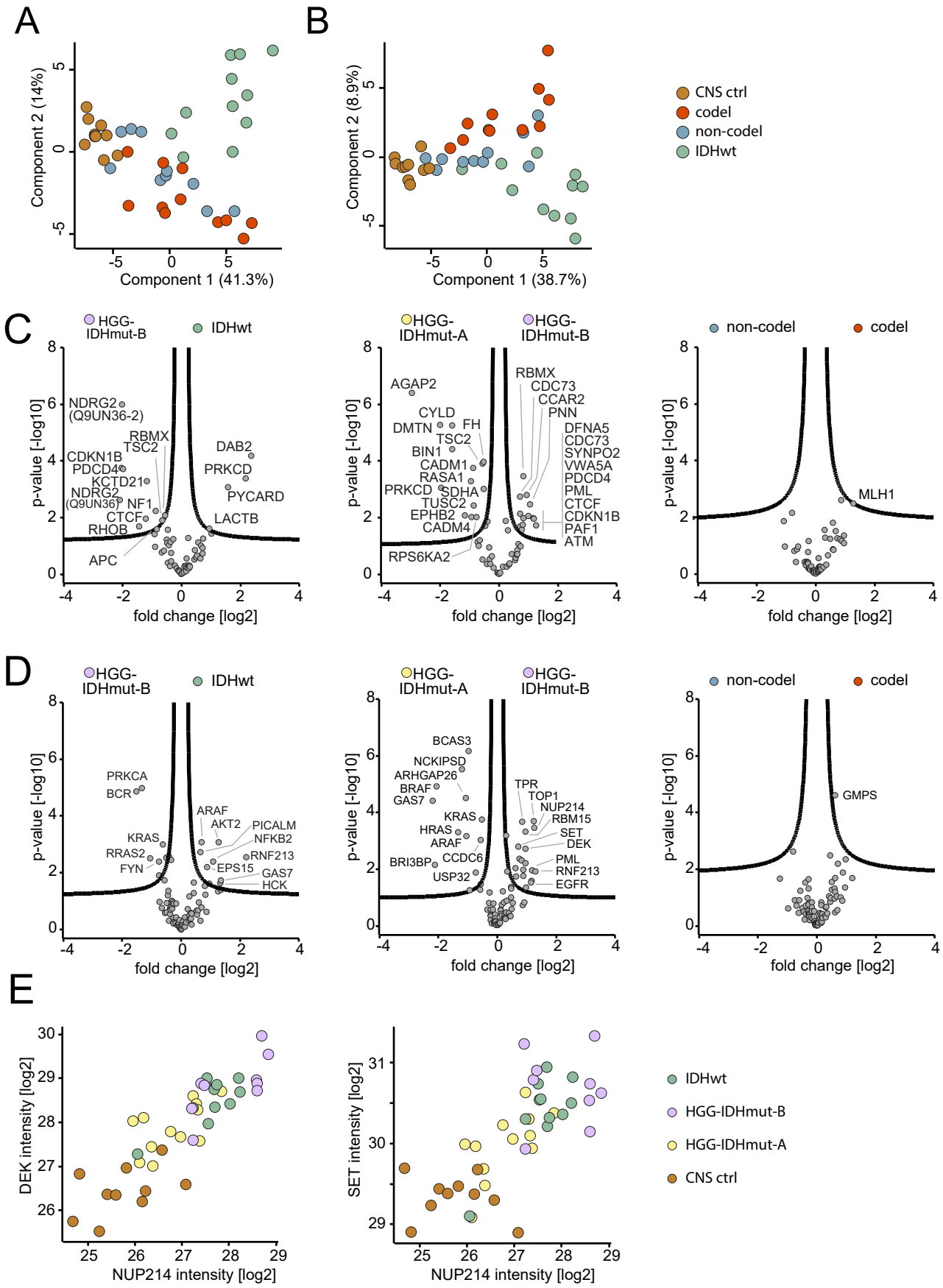
A
Component 2 (14%)
Component 1 (41.3%)
B
Component 2 (8.9%)
Component 1 (38.7%)
CNS ctrl
codel
non-codel
IDHwt
C
HGG-IDHmut-B
IDHwt
HGG-IDHmut-A
HGG-IDHmut-B
non-codel
codel
p-value [-log10]
fold change [log2]
NDRG2 (Q9UN36-2)
RBMX
TSC2
CDKN1B
PDCD4
KCTD21
NDRG2 (Q9UN36)
NF1
CTCF
RHOB
APC
DAB2
PRKCD
PYCARD
LACTB
AGAP2
CYLD
DMTN
FH
TSC2
BIN1
CADM1
RASA1
PRKCD
SDHA
TUSC2
EPHB2
CADM4
RPS6KA2
RBMX
CDC73
CCAR2
PNN
DFNA5
CDC73
SYNPO2
VWA5A
PDCD4
PML
CTCF
CDKN1B
PAF1
ATM
MLH1
D
HGG-IDHmut-B
IDHwt
HGG-IDHmut-A
HGG-IDHmut-B
non-codel
codel
p-value [-log10]
fold change [log2]
PRKCA
BCR
KRAS
RRAS2
FYN
ARAF
AKT2
PICALM
NFKB2
RNF213
EPS15
GAS7
HCK
BCAS3
NCKIPSD
ARHGAP26
BRAF
GAS7
KRAS
HRAS
ARAF
BRI3BP
CCDC6
USP32
TPR
TOP1
NUP214
RBM15
SET
DEK
PML
RNF213
EGFR
GMPS
E
DEK intensity [log2]
NUP214 intensity [log2]
SET intensity [log2]
NUP214 intensity [log2]
IDHwt
HGG-IDHmut-B
HGG-IDHmut-A
CNS ctrl

Figure S5. No separation of codel and non-codel entity in the tumor suppressor and proto-oncogene proteomes. Related to Figure 4.

A-B) Principal component analysis of UniProt Keyword-annotated tumor suppressor gene (A) and proto-oncogene (B) datasets. Samples, n=10 (ctrl CNS), n=11 (IDHwt), n=11 (codel), n=10 (non-codel).

C) Regulation of tumor suppressors between IDHwt and HGG-IDHmut-B (left), HGG-IDHmut-B and HGG-IDHmut-A (center), and codel and non-codel (right). Samples, n=10 (ctrl CNS), n=12 (HGG-IDHmut-A), n=9 (HGG-IDHmut-B), n=11 (IDHwt), n=11 (codel), n=10 (non-codel).

D) Regulation of oncoproteins between IDHwt and HGG-IDHmut-B (left), HGG-IDHmut-B and HGG-IDHmut-A (center), and codel and non-codel (right). Samples as in C.

E) Correlation of protein abundances of NUP214 and DEK (left), and NUP214 and SET (right) across samples. Pearson correlation coefficients r = 0.87 (left) and r = 0.76 (right). Samples as in C.

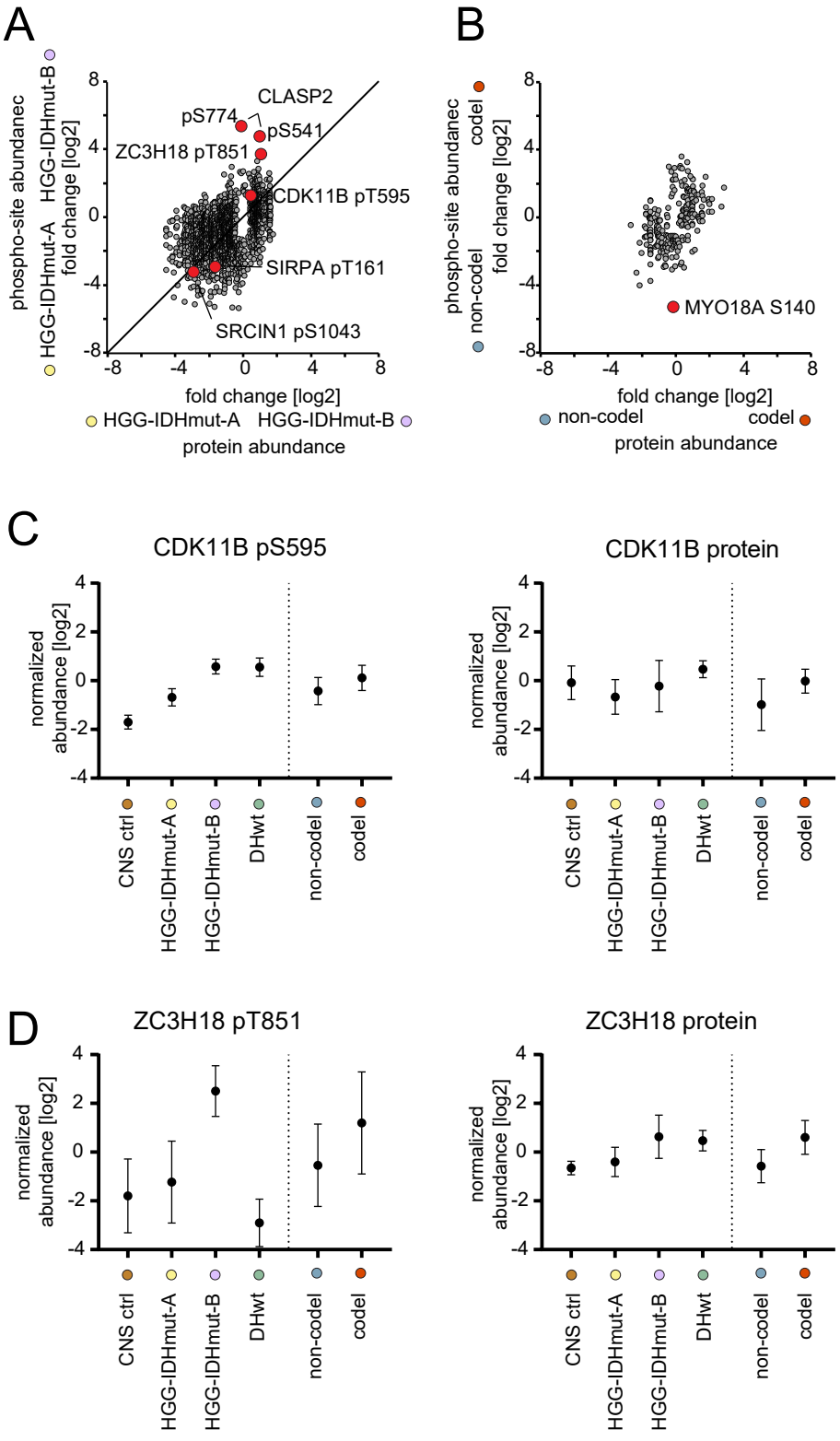
A
phospho-site abundanec
HGG-IDHmut-B
HGG-IDHmut-A
fold change [log2]
CLASP2
pS774
pS541
ZC3H18 pT851
CDK11B pT595
SIRPA pT161
SRCIN1 pS1043
fold change [log2]
HGG-IDHmut-A HGG-IDHmut-B
protein abundance
B
phospho-site abundanec
codel
non-codel
fold change [log2]
MYO18A S140
fold change [log2]
non-codel codel
protein abundance
C
CDK11B pS595
normalized abundance [log2]
CNS ctrl
HGG-IDHmut-A
HGG-IDHmut-B
DHwt
non-codel
codel
CDK11B protein
normalized abundance [log2]
CNS ctrl
HGG-IDHmut-A
HGG-IDHmut-B
DHwt
non-codel
codel
D
ZC3H18 pT851
normalized abundance [log2]
CNS ctrl
HGG-IDHmut-A
HGG-IDHmut-B
DHwt
non-codel
codel
ZC3H18 protein
normalized abundance [log2]
CNS ctrl
HGG-IDHmut-A
HGG-IDHmut-B
DHwt
non-codel
codel

Figure S6. Phosphosite dynamics in IDHmut glioma. Related to Figure 4.

A-B) Relationship of phosphosite abundance differences and protein abundance differences, each between HGG-IDHmut-B and HGG-IDHmut-A (A) and codel and non-codel (B). Outliers labelled in Fig. 4C also labelled here with gene name and phosphorylation site. Phosphorylation sites included if abundance difference in at least one dimension (phosphosite, protein) significant with q-value < 5% (A) or p-value < 0.05% (less stringent) (B). Diagonal line marks 1:1 relationship. Samples, n=12 (HGG-IDHmut-A), n=9 (HGG-IDHmut-B), n=11 (codel), n=10 (non-codel).

C-D) Abundance of CDK11B phosphorylation site pS595 (C) and ZC3H18 phosphorylation site pT851 (D) and protein abundances, respectively. Circles denote means and bars 95% confidence intervals of means. Samples, n=10 (ctrl CNS), n=12 (HGG-IDHmut-A), n=9 (HGG-IDHmut-B), n=11 (IDHwt), n=11 (codel), n=10 (non-codel).

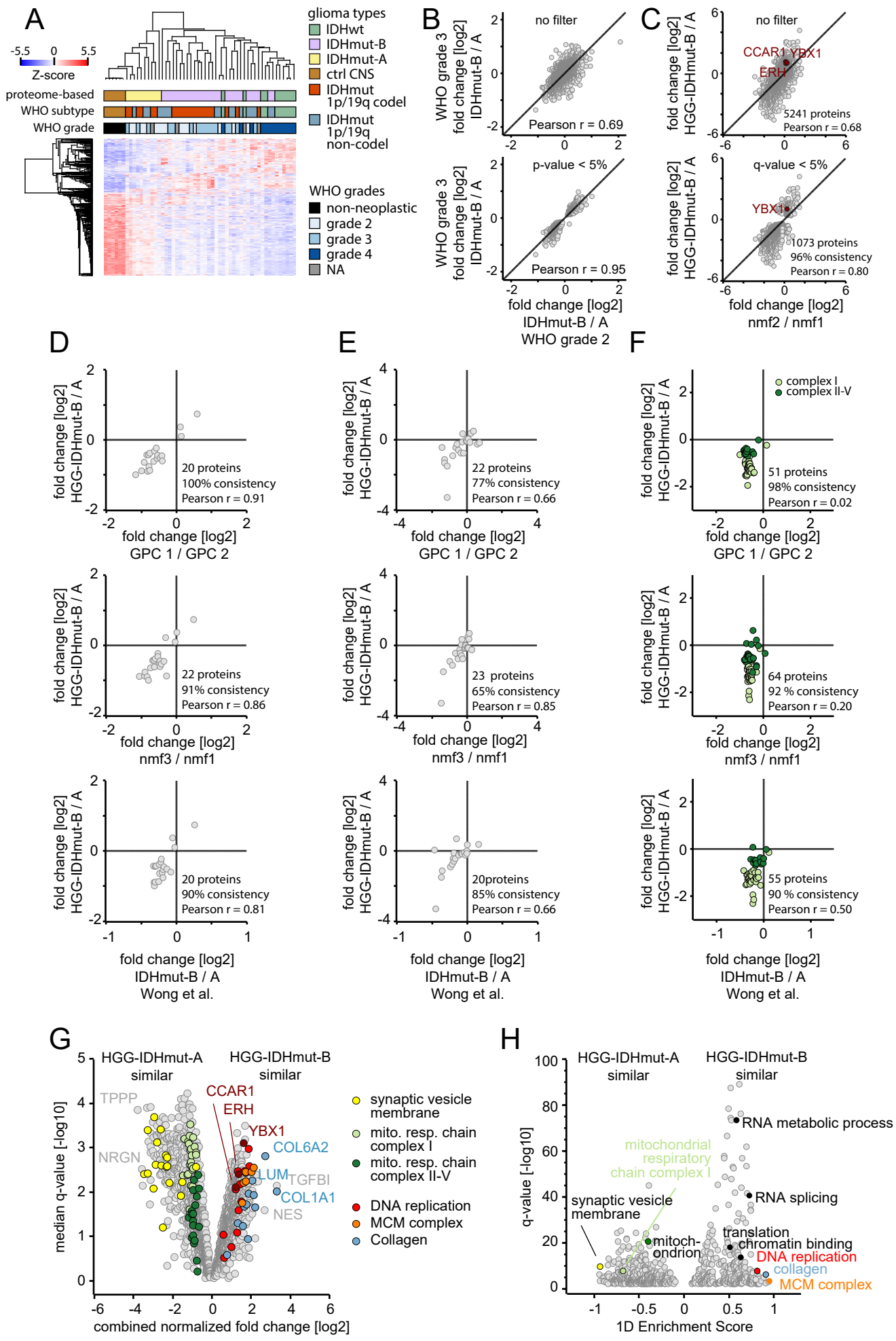
A
-5.5 0 5.5
Z-score
proteome-based
WHO subtype
WHO grade
glioma types
IDHwt
IDHmut-B
IDHmut-A
ctrl CNS
IDHmut 1p/19q codel
IDHmut 1p/19q non-codel
WHO grades
non-neoplastic
grade 2
grade 3
grade 4
NA
B
no filter
Pearson r = 0.69
p-value < 5%
Pearson r = 0.95
WHO grade 3 fold change [log2] IDHmut-B / A
fold change [log2] IDHmut-B / A WHO grade 2
C
no filter
CCAR1 YBX1
ERH
5241 proteins
Pearson r = 0.68
q-value < 5%
YBX1
1073 proteins
96% consistency
Pearson r = 0.80
fold change [log2] HGG-IDHmut-B / A
fold change [log2] nmf2 / nmf1
D
20 proteins
100% consistency
Pearson r = 0.91
22 proteins
91% consistency
Pearson r = 0.86
20 proteins
90% consistency
Pearson r = 0.81
fold change [log2] GPC 1 / GPC 2
fold change [log2] nmf3 / nmf1
fold change [log2] IDHmut-B / A Wong et al.
E
22 proteins
77% consistency
Pearson r = 0.66
23 proteins
65% consistency
Pearson r = 0.85
20proteins
85% consistency
Pearson r = 0.66
F
complex I
complex II-V
51 proteins
98% consistency
Pearson r = 0.02
64 proteins
92 % consistency
Pearson r = 0.20
55 proteins
90 % consistency
Pearson r = 0.50
G
HGG-IDHmut-A similar
HGG-IDHmut-B similar
TPPP
NRGN
CCAR1
ERH
YBX1
COL6A2
LUM
TGFBI
COL1A1
NES
median q-value [-log10]
combined normalized fold change [log2]
synaptic vesicle membrane
mito. resp. chain complex I
mito. resp. chain complex II-V
DNA replication
MCM complex
Collagen
H
HGG-IDHmut-A similar
HGG-IDHmut-B similar
RNA metabolic process
mitochondrial respiratory chain complex I
RNA splicing
synaptic vesicle membrane
translation
mitoch-ondrion
chromatin binding
DNA replication
collagen
MCM complex
q-value [-log10]
1D Enrichment Score

Figure S7. Integration of other proteomic glioma datasets. Related to Figure 5.

A) Identification of IDHmut-A and IDHmut-B in the Wong et al. dataset by Pearson coefficient-based hierarchical clustering of samples and ANOVA-significant (s0 = 2, q < 5%) proteins regulated by WHO-defined glioma subtype (IDHwt, IDHmut 1p/19 codel, IDHmut 1p/19q non-codel). Samples, n=6 (ctrl CNS), n=10 (IDHmut-A), n=28 (IDHmut-B), n=10 (IDHwt) and according to WHO classification n=21 (IDHmut 1p/19q-codeleted), n=17 (IDHmut non-codeleted, n=10 (IDHwt).

B) Comparison of fold changes between IDHmut-A and IDHmut-B in glioma samples in the Wong et al. dataset with WHO grade 2 (x axis, 6 IDHmut-A glioma, 9 IDHmut-B glioma) to those fold changes in glioma samples of WHO grade 3 (y axis, 3 IDHmut-A glioma, 13 IDHmut-B glioma) for all proteins (upper panel, 5897 proteins) and significantly regulated proteins (p < 5% in both comparisons, lower panel, 703 proteins). When filtering for significantly regulated proteins (p < 5%) in at least 1 of the two comparisons (within WHO 2, within WHO 3), 2050 proteins included and Pearson r = 0.81 (scatter plot not shown).

C) Comparison of fold changes between nmf2 ("mesenchymal-like", n=37) and nmf1 ("proneural-like, n=29) of the Wang et al./CPTAC dataset (x axis) and HGG-IDHmut-B (n=9) and HGG-IDHmut-A (n=12) in the dataset of this study (y axis) for all overlapping proteins (upper panel) and proteins significantly regulated (q < 5%) in both datasets.

D-F) Comparison of metabolic proteins across studies. Fold changes HGG-IDHmut-B (n=9) / HGG-IDHmut-A (n=12) (this study) compared to those of corresponding glioma subgroups GPC1 (n=26) / GPC2 (n=13) (Oh et al. dataset), nmf3 (n=25) / nmf1 (n=29) (Wang et al./CPTAC dataset), and IDHmut-B (n=28) / IDHmut-A (n=10) (Wong et al. dataset) for tricarboxylic acid cycle proteins (D), glycolysis proteins (E), and mitochondrial respiratory chain proteins (F).

G) Regulated proteins across four datasets in pseudo-Volcano plot. Proteins included were either consistenly enriched in HGG-IDHmut-B, nmf3, GPC1, IDHmut-B compared to HGG-IDHmut-A, nmf1, GPC2, IDHmut-A (dataset of this study, Wang/CPTAC et al., Oh et al., Wong et al.), respectively, or consistently inversely regulated. Sample numbers as in D-F. Protein fold changes normalized within each dataset after consistency filtering by division of mean (across proteins) absolute fold change separately for positive and negative fold changes. Subsequently, combined protein fold change (x axis) and q-value (y axis) calculated as median across the four studies.

H) Enrichment of functional protein annotation terms in the combined normalized fold change dimension of (G) by Perseus 1D Enrichment analysis. Terms displayed filtered for at least five member proteins and enrichment q-value of 1%.